

Numerical analysis of the Rayleigh–Taylor instability in an electric field

Qingzhen Yang^{1,2}, Ben Q. Li^{3,†}, Zhengtuo Zhao³, Jinyou Shao⁴
and Feng Xu^{1,2}

¹The Key Laboratory of Biomedical Information Engineering of Ministry of Education, School of Life Science and Technology, Xi'an Jiaotong University, Xi'an, Shaanxi 710049, PR China

²Bioinspired Engineering and Biomechanics Center (BEBC), Xi'an Jiaotong University, Xi'an, Shaanxi 710049, PR China

³Department of Mechanical Engineering, University of Michigan, Dearborn, MI 48128, USA

⁴State Key Laboratory for Manufacturing Systems Engineering, Xi'an Jiaotong University, Xi'an, Shaanxi 710049, PR China

(Received 18 October 2014; revised 6 January 2016; accepted 16 January 2016;
first published online 3 March 2016)

A numerical analysis is presented of the Rayleigh–Taylor instability (RTI) in the presence of an external electric field, with an emphasis on nonlinear phenomena associated with the evolution of complex interfacial morphology. The Poisson equation for the electric field and the Navier–Stokes equation for fluid flow field are solved simultaneously along with the Cahn–Hilliard phase field equation for interface deformation and morphology development. Numerical model is validated against the existing data and the results of linear analysis. Extensive numerical simulations are carried out for a wide range of fluid flow and electric field conditions. Computed results show that, in both linear and nonlinear regimes, a horizontal field suppresses the RTI, while a vertical electric field aggravates it. However, the vertical field does not affect the secondary instability; specifically, it does not contribute to the baroclinical generation of vorticity and consequently does not affect the roll-up formation. Linear analysis predicts that the RTI remains the same with the interchange of the dielectric constants of the two fluids, which is also confirmed by the numerical model for small interface deformations. This prediction, however, does not hold true in the nonlinear regimes in that complex interfacial morphology may evolve quite differently if the dielectric constants of two fluids are interchanged.

Key words: instability control, MHD and electrohydrodynamics, multiphase flow

1. Introduction

The Rayleigh–Taylor instability (RTI) occurs when a heavier fluid initially sits above a lighter one in a gravity field, which was first discovered by Rayleigh (1883, 1900) and later applied to all accelerated fluids by Taylor (1950). Small perturbations at the initially flat heavy/light fluid interface would set in the instability and evolve

† Email address for correspondence: benqli@umich.edu

into complex nonlinear structures in the form of ‘bubbles’ and ‘spikes’ (Sharp 1984). At the early stage the ‘bubble’ rises exponentially based on the linear mechanism, and then it attains a more realistic velocity as the nonlinear interaction comes into play. Eventually, vortex structures form around the ‘spikes’, leading to the RTI turbulent mixing (Chertkov 2003; Boffetta *et al.* 2009; Sohn 2009). Since the initial study on the RTI over a century ago, the topic has attracted continuous interest because both of its fundamental importance and of its widespread applications in the fields of geophysics (Michioka & Sumita 2005), astrophysics (Ribeyre, Tikhonchuk & Bouquet 2004) and inertial confinement fusion (Kilkenny *et al.* 1994).

Extensive research on the RTI has been carried out with theoretical, experimental and numerical approaches. Theoretical analysis was conducted first by Rayleigh (1883), who performed a linear stability analysis describing the early stage growth of the RTI initiated with a single mode perturbation under the gravitational force. More than half a century later, Taylor (1950) extended the model to the general stability cases of heterogeneous fluid accelerated in a direction perpendicular to the plane of stratification. Different theoretical models were also developed by other researchers (Sharp 1984; Kull 1991). Laboratory experiments were also conducted with focus on initial condition effects, late stage turbulent mixing and so on (Layzer 1955; Dalziel 1993; Schneider, Dimonte & Remington 1998; Dimonte & Schneider 2000; Olson & Jacobs 2009). Numerical simulation of the RTI has gained its popularity since 1980s (Youngs 1984; Tryggvason 1988). The RTI now has been considered as the benchmark of two-phase flow problems, and also used as the canonical case for different numerical studies (Ding, Spelt & Shu 2007). From the perspective of numerical simulation, the RTI falls into the category of free surface problem associated with two-phase flows. For the study of these problems, numerical methods have been developed including, but not limited to, the volume of fluid (VOF) method (Hirt & Nichols 1981), the finite element projection method (Guermont & Quartapelle 2000), the phase field method (Jacqmin 1999; Ding *et al.* 2007; Celani *et al.* 2009a) and the lattice Boltzmann method (Chen & Doolen 1998; He, Chen & Zhang 1999). Among these numerical treatments, phase field has been demonstrated to be effective and accurate in simulating the RTI (Jacqmin 1999; Ding *et al.* 2007; Celani *et al.* 2009b) and hence is employed in this study. While the RTI evolves from initial random perturbations (i.e. multiple interacting wavelengths), a single mode analysis is of fundamental importance as it serves as a foundation for more complex mathematical models of the multimode RTI (Dimonte 2004). Despite its apparent simplicity, the single mode RTI has not yet been well understood and continues to be the intensive research subject of experimental (White *et al.* 2010; Renault *et al.* 2011), numerical (Lee, Kim & Kim 2011; Ramaprabhu *et al.* 2012) and theoretical (Abarzhi 2010) studies.

It is well known that an imposed electric field would change the stability of an interface (Melcher & Schwarz Jr 1968; Craster & Matar 2009; Joshi, Radhakrishna & Rudraiah 2010). Grandison, Papageorgiou & Vanden-Broeck (2007, 2012) investigated the influence of an electric field on the Kelvin–Helmholtz instability (KHI), and found that a strong enough field could stabilize the system with the assistance of surface tension. Mohamed & El Shehawey (1983a,b) presented a weakly nonlinear analysis of perpendicular electric field on the RTI. Recently, Barannyk, Papageorgiou & Petropoulos (2012) studied the suppression effect of horizontal electric field on the RTI, assuming that the fluids are inviscid and the flow is irrotational. Both initial value problem and travelling waves were discussed. Korovin (2011) considered a perturbation as a 2-D planar surface wave in the RTI with the presence of a

tangential electric field, and discussed the effect of the angle between the field and surface wave vector. Recently it was found that the instability of a polymer interface in perpendicular electric field could be used to generate the micro/nano patterning in a polymer film (Wu & Russel 2009).

There appears to have been little work on the nonlinear effects of electric field on the RTI, with exceptions given by Cimpeanu, Papageorgiou & Petropoulos (2014) and Rahmat *et al.* (2014). The former is concerned with stability and growth rates in a horizontal electric field, and the effect of electric field on the interfacial morphology is not studied. The latter, on the other hand, deals with electrically conducting fluids only. The present study is concerned about the effect of the electric field on the RTI, focused on the nonlinear phenomena and the associated interfacial morphology development driven by a combined effect of gravity and an external electric field. This paper is organized as follows. The mathematical model, along with governing equations, is given first and the numerical solution methodology is described. Having validated the model, numerical simulations were conducted to determine the effect of physical quantities on the nonlinear interactions characterizing the electrohydrodynamic RTI, such as the electric field (including the orientation and strength), surface tension and viscosity. Computed results are presented showing that for two dielectric fluids in a Rayleigh–Taylor system, a vertical electric field not only aggravates the RTI but also weakens the roll-ups at the falling tip. In addition, the permittivity ratio of the two liquids can have a profound effect on the nonlinear development of interface deformation and morphologies.

2. Mathematical model

The problem under consideration is sketched in figure 1, where two immiscible viscous and incompressible fluids are confined in an infinite horizontal channel with the depth of l . The density, viscosity and electrical permittivity of the fluids are ρ_i , μ_i and ε_i ($i = 1, 2$), respectively. Both fluids are dielectric materials separated by a charge-free interface. The surface tension coefficient between the two fluids is represented by γ . As usual, the upper fluid bears a larger density $\rho_1 < \rho_2$, which is susceptible to the classical RTI: the amplitude would be amplified if a perturbation arises on the interface. An electric field is imposed upon the system. The evolution of the interfacial morphology under the influence of the electric field is the subject of numerical analysis in this paper. In figure 1, both the horizontal and vertical fields are plotted for the sake of illustration. These two cases will be discussed separately.

The details of the numerical model have been described elsewhere (Yang *et al.* 2014); thus only a brief account is given here. The phase field as an effective tool for modelling the free surface problem has been employed to study the classical RTI (Jacqmin 1999; Ding *et al.* 2007; Celani *et al.* 2009b). The phase field, electric field and fluid flow field are governed by the equations described below.

2.1. Phase field equation

In the phase field, a phase parameter C is introduced such that $C = 1$ and $C = 0$ correspond to two distinctive phases, respectively. The evolution of the phase parameter C traces out the deformation of the free surface. For the problem considered in this study, both diffusion and convection effects contribute to the development of phase field. The convective Cahn–Hilliard equation (Jacqmin 1999) is employed here to describe the evolution of the phase field,

$$C_t + \mathbf{u} \cdot \nabla C - M \nabla^2 \phi = 0 \quad \in \Omega \times T, \tag{2.1}$$

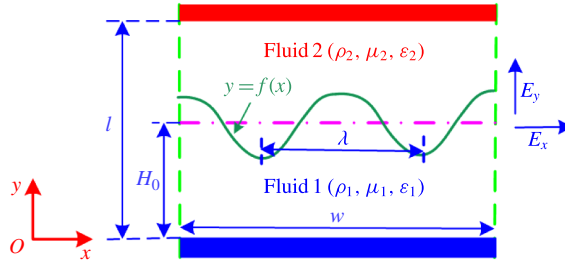


FIGURE 1. (Colour online) Schematic of the electrohydrodynamic RTI problem, the lower left corner is chosen as the original point of the coordinate. The electric field is in either horizontal or vertical direction.

where Ω is the geometric computational domain, with its boundary defined by $\partial\Omega$, T is the computing time duration, \mathbf{u} represents the fluid velocity, M is the phase field mobility and is taken as a constant in this study and ϕ is the chemical potential which is defined as $\phi = \delta f / \delta C$. The free energy density function, f , which is a function of phase parameter C , takes the following form,

$$f(C) = \frac{1}{2}\xi\gamma\alpha|\nabla C|^2 + \xi^{-1}\gamma\alpha \cdot \frac{1}{4}C^2(1 - C)^2 \quad \in \Omega \times T, \tag{2.2}$$

where γ is the surface tension coefficient, ξ is a measure of interface thickness and $\alpha = 6\sqrt{2}$ is a constant.

2.2. Electric field equation

In dielectric materials, an external electric field polarizes the molecules, and the molecular dipoles so induced in return modifies the electric field. The resulting electric field is governed by the Gauss law $\nabla \cdot (\epsilon_r(C)\mathbf{E}) = q^e$ (Jackson 1999), where $\epsilon_r(C)$ is the relative dielectric permittivity, \mathbf{E} electric field intensity and q^e free charge density. In this study, we focus on the fluids with small conductivity (e.g. benzene). For the case under consideration, the time scale of the flow $t_c = L_c/U_c$ (L_c being the length scale and U_c the characteristic velocity) is much smaller than that of the charge relaxation $t_\sigma = \epsilon_0\epsilon_r/\sigma$ ($t_c \ll t_\sigma$ or $\sigma \ll \epsilon_0\epsilon_r U_c/L_c$). As a result, the free charge may be neglected in the media ($q^e = 0$), and only polarized charges need to be counted for the electrical performance during the process.

Within the framework of electrohydrodynamics, the dynamic current is small, and hence the magnetic field is negligible. Also, the curl of the electric field is approximately zero ($\nabla \times \mathbf{E} = 0$), which allows us to write $\mathbf{E} = -\nabla V$ (where V is the electric potential). Thus the governing equation of the electric field reduces to the Laplace equation (Tomar *et al.* 2007; Hua, Lim & Wang 2008; Lin, Skjetne & Carlson 2012),

$$\nabla \cdot (\epsilon_r(C)\nabla V) = 0 \quad \in \Omega \times T. \tag{2.3}$$

The above equation governs both the bulk fluids and the diffuse interface. Indeed, one of the merits of phase field model is that, by introducing the phase parameter C , the entire domain can be treated in a unified manner. This is in contrast with a sharp interface model where the two fluids must be treated separately, and a jump boundary condition is necessary at the fluid/fluid interface. Compared with the conventional Laplace equation ($\nabla^2 V = 0$), the permittivity $\epsilon_r(C)$ in (2.3) is not a constant but a variable that depends on the phase parameter C . Thus for a two-phase flow problem, such as the RTI, the permittivity $\epsilon_r(C)$ varies spatially.

2.3. Flow field equation

The flow field is described by the governing equations of mass conservation and momentum balance equations. Both fluids are considered as incompressible, (Ding *et al.* 2007)

$$\nabla \cdot \mathbf{u} = 0 \quad \in \Omega \times T. \tag{2.4}$$

The Navier–Stokes equations should be modified to allow for variable density and viscosity. For the present study, the external force includes the gravitational force, electrical force and surface tension force on the interface. Thus, the vector momentum balance equation takes the form of

$$\rho(C)(\mathbf{u}_t + \mathbf{u} \cdot \nabla \mathbf{u}) = -\nabla p + \nabla \cdot [\mu(C)(\nabla \mathbf{u} + \nabla \mathbf{u}^T)] + \rho(C)\mathbf{g} + \mathbf{f}_\gamma + \mathbf{f}_e \quad \in \Omega \times T, \tag{2.5}$$

where \mathbf{f}_e denotes the electrical force (Tomar *et al.* 2007; Hua *et al.* 2008; Lin *et al.* 2012), \mathbf{f}_γ accounts for the surface tension force, \mathbf{g} is the gravity acceleration, $\rho(C)$ is the density of fluid, p is the pressure and $\mu(C)$ is the viscosity. Note that (2.5) is valid for the entire computational domain, which is made possible by letting the physical properties be a function of the phase parameter C . The surface tension force is expressed as

$$\mathbf{f}_\gamma = \phi \nabla C \tag{2.6}$$

with ϕ being the chemical potential. The electrical force \mathbf{f}_e can be calculated by taking the divergence of the Maxwell stress tensor (Saville 1997):

$$\begin{aligned} \mathbf{f}_e &= \nabla \cdot \left\{ \varepsilon_0 \varepsilon_r \mathbf{E} \mathbf{E} - \frac{1}{2} \varepsilon_0 \varepsilon_r \left[1 - \frac{\rho}{\varepsilon_r} \left(\frac{\partial \varepsilon_r}{\partial \rho} \right)_T \right] \mathbf{E} \cdot \mathbf{E} \boldsymbol{\delta} \right\} \\ &= \nabla \cdot \left[\varepsilon_0 \varepsilon_r \mathbf{E} \mathbf{E} - \frac{1}{2} \varepsilon_0 \varepsilon_r \mathbf{E} \cdot \mathbf{E} \boldsymbol{\delta} \right] + \varepsilon_0 \nabla \left(\frac{1}{2} \mathbf{E} \cdot \mathbf{E} \frac{\partial \varepsilon_r}{\partial \rho} \rho \right), \end{aligned} \tag{2.7}$$

where \mathbf{E} is the electric field intensity, and $\boldsymbol{\delta}$ the identity matrix. In the above equation, the first term on the right-hand side represents the electrical force due to the electrical charge, which sometimes is referred to as the Korteweg–Helmholtz force. The second one originates from the changes in material density, usually referred to as the electrostriction force density. This term is neglected in this paper as the fluid is incompressible.

2.4. Dimensionless parameters

In order to represent the density difference, the Atwood ratio $A = (\rho_2 - \rho_1)/(\rho_2 + \rho_1)$ is introduced, which is a key factor governing the RTI. The governing equations are normalized by the characteristic parameters: length L_c , velocity $U_c = \sqrt{AgL_c}$, and time $t_c = L_c/U_c = \sqrt{L_c/Ag}$. Furthermore, the following dimensionless parameters are defined to simplify the analysis of the problem,

$$Re = \frac{\rho_m \sqrt{L_c^3 g}}{\mu_m}, \quad We = \frac{\gamma}{\rho_m g L_c^2}, \quad E_b = \frac{\varepsilon_0 \varepsilon_m V_0^2}{\rho_m g L_c w^2}, \quad Pe = \frac{\xi \sqrt{L_c^3 g}}{M \gamma}, \quad Cn = \frac{\xi}{L_c}, \tag{2.8a-e}$$

where subscript m ($= 1, 2$) stands for the fluid with a greater value; for instance, $\varepsilon_m = \varepsilon_2$ when $\varepsilon_2 > \varepsilon_1$. The Reynolds number (Re) describes the relative importance between the inertial (i.e. gravity) and the viscous force. Since gravity is a crucial force in the RTI, the significance of other forces is measured by dimensionless parameters in

relation to gravity. The Weber number (We) reveals the relative magnitude of interface tension force and gravity force. The electrical Weber number (E_b) describes the ratio of the electrical over the gravity force. It is worth noting that for a vertical electric field $E_b = \varepsilon_0 \varepsilon_m V_0^2 / (\rho_m g L_c l^2)$. The viscosity and electrical permittivity ratios of the two fluids are represented by $\lambda_\mu = \mu_2 / \mu_1$ and $\lambda_\varepsilon = \varepsilon_2 / \varepsilon_1$, respectively. For the phase field, two more parameters need to be defined: the Peclet number (Pe), which characterizes the ratio of the convective over diffusive mass transport and the Cahn number, Cn , which is defined as the ratio of the interface thickness over the characteristic length. For the problem in study, the two fluids are confined between two plates with a distance l . This height l is of importance and the characteristic length is chosen as $L_c = l/4$, also we assume $w = \lambda = l/4$ as the default value.

With the dimensionless parameters defined above, the governing equations can be normalized, namely,

$$C_t + \mathbf{u} \cdot \nabla C - \frac{1}{Pe} \nabla^2 \phi = 0, \quad (2.9a)$$

$$\nabla \cdot (\varepsilon_r(C) \nabla V) = 0, \quad (2.9b)$$

$$\nabla \cdot \mathbf{u} = 0, \quad (2.9c)$$

$$\begin{aligned} A\rho(C)[\mathbf{u}_t + (\mathbf{u} \cdot \nabla)\mathbf{u}] = & -\nabla p + \frac{\sqrt{A}}{Re} \nabla \cdot [\mu(C)(\nabla\mathbf{u} + \nabla\mathbf{u}^T)] + \rho(C)\mathbf{j} \\ & - \frac{1}{2}E_b\beta^2|\nabla V|^2\nabla\varepsilon_r(C) + We\phi\nabla C, \end{aligned} \quad (2.9d)$$

where $\phi = \delta f / \delta C$ and $f(C) = (1/2)\alpha|\nabla C|^2 Cn + (1/4Cn)\alpha C^2(1-C)^2$. Also, β is a shape factor with $\beta = w/L_c$ for a horizontal electric field, and $\beta = l/L_c$ for a vertical electric field. The dimensionless density, viscosity and relative permittivity are further given by

$$\rho(C) = (2AC + 1 - A)/(1 + A), \quad (2.10a)$$

$$\mu(C) = C + (1 - C)/\lambda_\mu, \quad (2.10b)$$

$$\varepsilon_r(C) = C + (1 - C)/\lambda_\varepsilon. \quad (2.10c)$$

2.5. Boundary and initial conditions

For the fluid flow field, no-slip conditions are imposed at the top and bottom walls, $\mathbf{u} = 0$ and the Neumann conditions are applied at side boundaries, $\partial\mathbf{u}/\partial n = 0$. For the electric field imposed in the vertical direction, Dirichlet boundary conditions are applied on a pair of electrodes, $V = 1$ at $y = l/L_c$, and $V = 0$ at $y = 0$, and Neumann conditions for the side boundaries, $\partial V/\partial n = 0$ at $x = 0$ and $x = 1$. For the horizontal electric field, the boundary conditions are different: $V = 1$ at $x = 0$, $V = 0$ at $x = 1$, and $\partial V/\partial n = 0$ at $y = l/L_c$ and $y = 0$. For pressure, its normal derivatives are all set to zero, $\partial p/\partial n = 0$. The Neumann boundary conditions are imposed at all boundaries for phase field and chemical potential, $\partial C/\partial n = 0$, and $\partial\phi/\partial n = 0$; this guarantees the conservation of total mass. Initially, the flow field is set zero everywhere, which means the system starts to evolve from quiescence. The initial interface is assumed to take a shape of a cosine wave, below which the phase parameter is set as $C = 0$ and above which $C = 1$.

2.6. Numerical methodology

All the equations are discretized by the finite difference method and solved numerically for each time step. The detailed computational methodology is described

elsewhere (Yang *et al.* 2014) and thus only an outline is given here. A collocated grid is used and the temporal terms in the above equations are discretized explicitly. Calculations start with the solution of the phase field C . Then, the density, viscosity and dielectric constant are updated using (2.9). In the present model, all the parameters (the density $\rho(C)$, viscosity $\mu(C)$ and permittivity $\varepsilon_r(C)$) are treated as linear functions of the phase parameter C across the interface. The specific form of the function is insignificant for the problem under consideration since the interface is rather thin compared with the whole computational domain. The first-order derivative terms employ an upwinding scheme to increase the numerical stability. The Laplace equation for the electric field is discretized using a central difference scheme and solved by the method of successive over-relaxation (SOR).

A projection method (Yang *et al.* 2014) is employed to solve the Navier–Stokes equation together with the mass conservation equation and with the force terms obtained from the electric field. For a large density ratio, spurious currents may occur at the interface, which may cause numerical instability. Numerical experience suggests that the harmonic interpolation, $1/\rho_{i+1/2} = (1/\rho_i + 1/\rho_{i+1})/2$, is useful in preventing this numerical instability (Yang, Li & Ding 2013) and it is thus used in the present study. Having obtained the fluid flow field, the phase field is then solved again for the next time step. This procedure repeats itself until the preset time duration is reached. The time steps and grid sizes are so chosen to ensure the accurate and stable numerical solutions.

3. Results and discussion

3.1. Model validation

Unless otherwise indicated, all the results in the following will be presented in dimensionless units introduced in the previous section. To validate our model, the classical RTI without electric field was simulated, and then compared against the available numerical results. The same parameters are chosen as given by Ding *et al.* (2007). Specifically, the Atwood ratio $A = 0.50$, $Re = 3000$, the height $l = 4w$, surface tension is not considered and the fluids are assumed to be incompressible. In the present case of zero surface tension, the Cahn–Hilliard equation simply amounts to the interface tracking only. The initial interface being located in a rectangular domain $[0, 1] \times [0, 4]$ at $y(x) = 2 + 0.1 \cos(2\pi x)$, which represents a planar interface superimposed by a perturbation of wavenumber $k = 1$ with an amplitude $0.1w$. The top of the rising fluid and the bottom of the falling fluid are monitored, with the results presented in figure 2. As can be seen, the computed results from the present model agree well with those of Ding *et al.*

After validating the numerical model for the conventional RTI without an electric field, the next step is to verify its correctness with the presence of an electric field. To do so, the results from numerical simulations are compared against those by linear stability analysis for the growth rate of RTI in a horizontal electric field (see appendix A for detailed linear stability analysis). Substituting the parameters into (A 14), the results by linear stability analysis are obtained and shown in figure 3, where the numerical results from the present model are also given. For this case, the gravity is ignored, which is equivalent to removing the term $\rho(C)\mathbf{j}$ from (2.9d). One detail needs to be clarified about the neglecting of gravity in this particular case. To maintain the same definition of the dimensionless parameters involving gravity (such as the Reynolds number), g is kept as a constant and assigned a value of $g = 9.8$. The interface is assumed to be $f(x, t) = e^{st}A_0 \cos(kx)$, and the real part of s represents the

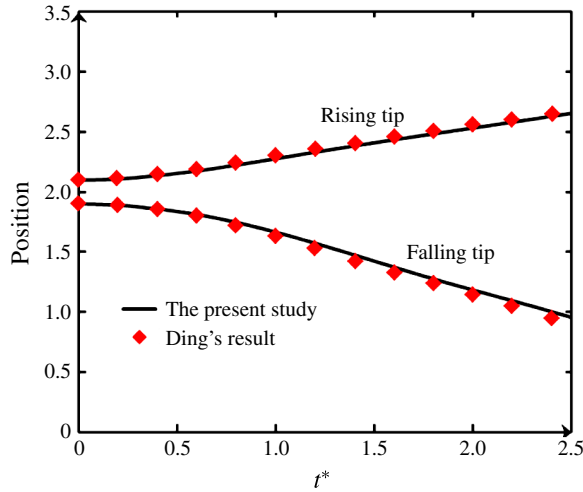


FIGURE 2. (Colour online) Time evolution of the positions of rising and falling tips, along with the results given by Ding *et al.* Both time and position are dimensionless.

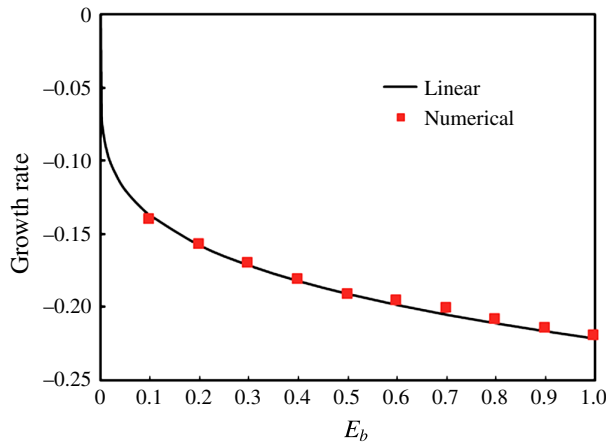


FIGURE 3. (Colour online) Comparison of the growth rates of interface perturbation predicted by linear stability analysis and by the present numerical model for horizontal electric fields imposed. Gravity and surface tension are ignored, and other parameters are listed in table 1. The growth rate is normalized by $t_c^{-1} = \sqrt{Ag/L_c}$.

growth rate of the perturbation. As shown in figure 3, s is negative, indicating that the instability is suppressed by the horizontal electric field. It is noted that the numerical data in figure 3 was obtained via the best fit of function $f(x, t)$. As it can be seen, the numerical results compare well with those of the linear analysis, validating the correctness of numerical phase field model. It is worth pointing out that in order to compare with linear stability analysis, the initial amplitude of perturbation A_0 is set sufficiently small for it to fall into the linear region (i.e. $A_0 \ll \lambda$, $\lambda = 2\pi/k$). More comparisons between the numerical and linear results are presented in the subsequent sections.

Parameters	Value
Reynolds number (Re)	1000
Atwood ratio (A)	0.50
Weber number (We)	0.001
Cahn number (Cn)	0.03
Ratio of viscosity (λ_μ)	1
Ratio of electrical permittivity (λ_ϵ)	3
Ratio of height/width (l/w)	4

TABLE 1. Parameters used in calculations.

For convenience, a set of default parameters are defined and listed in table 1. These values of parameters were used in the results to follow unless otherwise indicated. In the present study, the Peclet number (Pe) is taken as a function of surface tension $Pe = 2.5/\gamma$. If the surface tension is zero, the Peclet number would lose its meaning and phase field simply tracks the interface evolution caused by convection.

3.2. Stability analysis

3.2.1. Electrohydrodynamic RTI in a horizontal electric field

The effect of a horizontal electric field on the RTI is assessed in this section. It is known that a tangential electric field stabilizes the interface between two dielectric materials (Melcher & Schwarz Jr 1968). For the specific case of the RTI, according to the linear stability analysis, the horizontal electric field would suppress the perturbation on the interface (Barannyk *et al.* 2012). In the following, the numerical model described and validated above is employed to conduct the fully nonlinear analysis.

In the phase field model, the interface is represented by the contour of phase parameter $C = 0.5$. The initial perturbation is set as $y(x) = 2 + 0.0025 \cos(2\pi x)$. As the interface deformation evolves, the positions of ‘rising tip’ (i.e. bubble) and ‘falling tip’ (i.e. spike) are monitored. For the convenience of subsequent discussion, a parameter Δh is defined to quantitatively characterize the instability. This important quantity stands for the structure height, which is the difference between the positions, *viz.*

$$\Delta h = y_r - y_f, \tag{3.1}$$

where y_r and y_f measure the vertical positions of the rising and falling tips, respectively. A small Δh means the interface deformation is small, while a large value indicates a serve deformation.

The configuration being studied is shown in figure 1 with the electric field applied in the horizontal direction. For this case, both gravity and surface tension are considered. Computed results are plotted in figure 4(a), which shows the time change of structure height with different electric fields whose strength is characterized by the electrical Weber number E_b . Clearly, the instability is driven by a competing mechanism between the gravity and the horizontal electric field, with the former destabilizing the interface and the latter (electric field) stabilizing it. For the field-free case ($E_b = 0$), the gravity effect dominates and the structure height grows continuously and the instability is aggravated. A weak electric field slows down the instability but does not suppress it, which is evident with the cases of $E_b = 0.25$. However, a strong

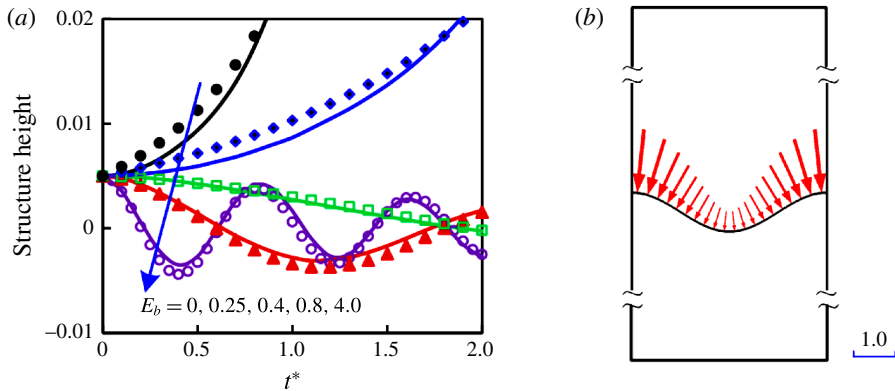


FIGURE 4. (Colour online) (a) Time evolution of structure height as affected by horizontal electric fields (E_b). The electrical permittivity ratio of the two fluids is $\varepsilon_2/\varepsilon_1 = 3:1$. Other parameters are the same as in table 1. Solid lines represent numerical results and discrete dots indicate linear analysis. (b) The electrical force distribution along the fluid–fluid interface. The scale bar measures the magnitude of the electrical force.

electric field (i.e. a large E_b) overwhelms the destabilizing effect of gravity and completely suppresses the interface perturbation. For the cases considered, with a field strength of $E_b = 0.4$, the perturbation is suppressed by the horizontal electric field. Moreover, an oscillation occurs during the suppression process, which is also reported in a previous study (Cimpeanu *et al.* 2014). For an even stronger electric strength ($E_b = 0.8$ and 4.0), the perturbation decays faster and the period of oscillation becomes shorter. For a comparison, the linear analysis results (see appendix A) are also shown in figure 4; clearly, the numerical results are consistent with the linear analysis. From the computed data, one may readily construct a stability diagram demarcating the stable and unstable regions, the boundary of which is defined by the critical voltage. According to the present calculations, the critical value of E_b is 0.32. This is in consistency with the critical value of $E_b = 0.3$ predicted by linear stability analysis (see appendix A for details).

To provide a better physical insight into the suppression effect of a horizontal electric field, the distribution of the electrical force (which in this case is referred as the Korteweg–Helmholtz force) along the interface is plotted in figure 4(b). It is noted that the plotted electrical force is normalized by $\varepsilon_0|\varepsilon_2 - \varepsilon_1|V_0^2/(2w^2)$, which is the force on a flat interface. In phase field representation, the fluid–fluid interface is characterized by a diffusive interface layer, whose thickness is defined by $0.01 \leq C \leq 0.99$ (C is the phase parameter). This is in contrast with a sharp interface model across which flux experiences a jump. The electrical force given in figure 4(b) is calculated by integrating the force density across the thickness of the diffusive interface layer, whose shape is given by $y(x) = 2 + 0.0025w \cos(2\pi x)$ at the onset of the instability. Although the force distribution evolves with time, a snap shot at an instant provides useful information on how it affects the interface development. As it is seen in figure 4(b), the force is normal to the interface and points downwards. It is strong at the rising tips on the two sides of the domain, pushing the interface downwards. At the falling tip, on the other hand, the electric force is weak. Also, the fluids are incompressible and need to satisfy the constraint of mass conservation. As a result, the interface is pushed upwards. This is the mechanism by which a horizontal electric field suppresses the RTI.

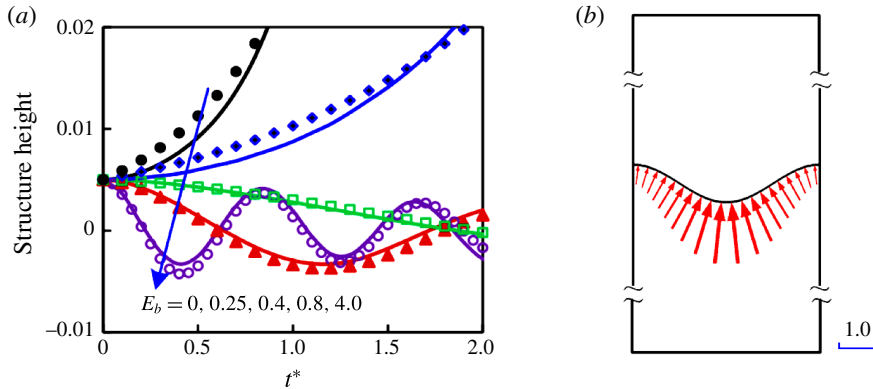


FIGURE 5. (Colour online) (a) Evolution of structure height under the influence of horizontal electric fields (E_b). The electrical permittivity ratio is $\varepsilon_2/\varepsilon_1 = 1 : 3$. Other parameters are the same as in table 1. Solid curves – numerical results and discrete dots – linear analysis. (b) The distribution of the electrical force along the interface. The scale bar denotes the magnitude of the electrical force.

The Korteweg–Helmholtz force is known being normal to the interface and pointing from the fluid with larger permittivity to the smaller one, thus the force depends on the relative values of the electrical permittivities of the two fluids. In the previous section, $\varepsilon_2 > \varepsilon_1$ was discussed. The case of $\varepsilon_2/\varepsilon_1 = 1 : 3$ is considered here. Figure 5(a) shows the evolution of structure height with different electrical Weber numbers. The results are similar to the case of $\varepsilon_2/\varepsilon_1 = 3 : 1$; namely, a weak horizontal electric field slows down the instability and a field strong enough can completely suppress it. The electrical force along the interface is displayed in figure 5(b). In contrast to figure 4(b), the force in this case points upward, being the largest at the falling tip and gradually decreasing from the falling to the raising tip along the interface. Under the action of this electrical force (figure 5b), the falling tip is pushed upward and the rising tip is squeezed downward due to the conservation of mass, thereby resulting in a suppression effect on the instability.

For both $\varepsilon_2/\varepsilon_1 > 1$ and $\varepsilon_2/\varepsilon_1 < 1$, a horizontal electric field produces a suppression effect on the RTI. The suppression effect is also predicted by a linear stability analysis (see appendix A for details), where the effect of the electric field in the dispersion equation appears as $\varepsilon_0(\varepsilon_2 - \varepsilon_1)^2 E_0^2 / (\varepsilon_2 + \varepsilon_1)$ (see (A 14)). This term remains the same for both $\varepsilon_2 > \varepsilon_1$ and $\varepsilon_2 < \varepsilon_1$, but it produces an opposite effect to gravity. The reason of comparing the two cases ($\varepsilon_2/\varepsilon_1 = 3 : 1$ and $1 : 3$) is to indicate that the stability characteristic resembles each other for the two cases but the detailed action of the electric forces on the interface is different. Also, the interfacial morphology differs for the two cases, which may not be explained by linear analysis, as it will be discussed in § 3.3.

3.2.2. Electrohydrodynamic RTI in a vertical electric field

The electric field in different orientations has different effects on the interface instability. It is known that the electric field perpendicular to the interface would aggravate the instability (Taylor & Mcewan 1965). Recently this phenomenon is exploited to manufacture the micro/nano structure on thin polymer films (Wu & Russel 2009). In this section, the effect of a vertical electric field on the RTI is

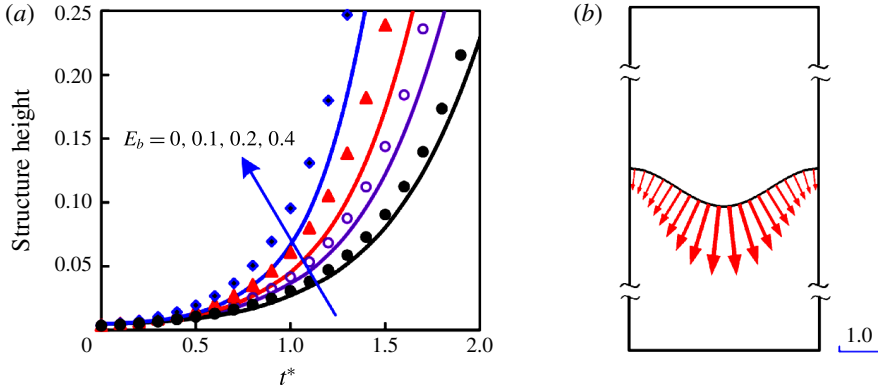


FIGURE 6. (Colour online) (a) Evolution of structure height under the action of vertical electric fields (E_b). The electrical permittivity ratio is $\varepsilon_2/\varepsilon_1 = 3:1$. Other parameters are the same as in table 1. Solid lines represent numerical results and discrete dots indicate linear analysis. (b) The electrical force distribution along the interface. The scale bar indicates the magnitude of the electrical force.

discussed. Consistent with the previous section, the structure height is monitored during numerical simulation in order to quantify the instability. The case of $\varepsilon_2/\varepsilon_1 = 3:1$ is studied first, and the results are plotted in figure 6. Both numerical and linear analytical results are depicted in figure 6. As expected, they agree with each other when the structure height is small; and deviate from each other for a large structure height as the nonlinear effect comes into play. Clearly, both numerical and linear analytical results indicate that the vertical electric fields tend to enhance the RTI. The structure height accelerates higher in time with a vertical electric field, and the interface becomes more and more unstable with an increase in the electric field strength. The stability analysis in a vertical electric field can also be performed by a linear theory (see appendix B for details), which yields the same conclusion. In an attempt to uncover the mechanism for this effect, the electrical force distribution along the interface is depicted in figure 6(b). The force acts downward with a maximum at the falling tip and gradually reduces in magnitude along the interface to a minimum at the rising tip. For the vertical electric field, the electrical forces are normalized by $\varepsilon_0|\varepsilon_2 - \varepsilon_1|V_0^2/(2l^2)$. Following the same line of argument as discussed in the above, the force distribution in figure 6(b) accelerates the downward motion of the interface at the falling tip and the upward motion at the rising tip due also to the conservation of mass, thereby enhancing the RTI.

The case of $\varepsilon_2/\varepsilon_1 = 1:3$ is shown in figure 7(a), where similar results are obtained, that is, the RTI is enhanced and becomes stronger with a larger electrical Weber number. Electrical force along the interface at the initial occasion is plotted in figure 7(b). The orientation and the distribution of the electrical force along the interface both are almost opposite to those in the case of $\varepsilon_2/\varepsilon_1 = 3:1$. The force points upwards with the largest value at the rising tip and the smallest one at that falling part, which, in combination with the requirement for mass conservation, results in an aggravation of the RTI.

3.3. Interfacial morphology of electrohydrodynamic RTI

The RTI usually evolves in the following pattern: one part of fluids falls downward (sometimes referred as ‘spike’) while the other rises up (i.e. ‘bubble’), with sometimes

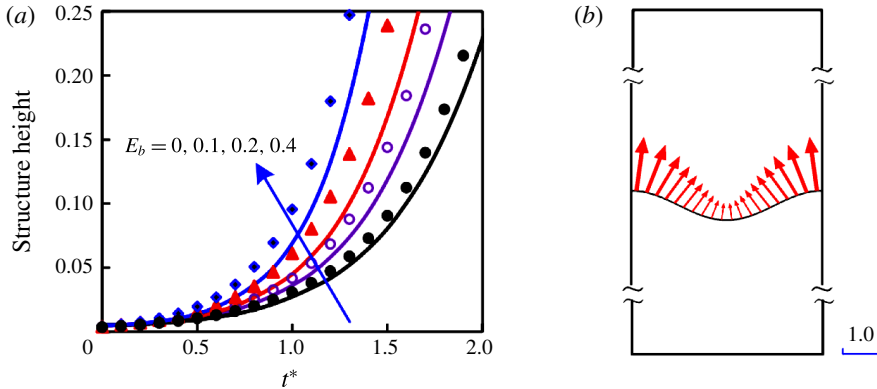


FIGURE 7. (Colour online) (a) Evolution of structure height under the action of vertical electric fields (E_b). The electrical permittivity ratio is $\varepsilon_2/\varepsilon_1 = 1 : 3$. Other parameters are the same as in table 1. Solid curves – numerical results and discrete dots – linear analysis. (b) The electrical force distribution along the interface. The scale bar denotes the magnitude of the electrical force.

roll-ups appearing at the tip due to nonlinear interaction (Sharp 1984). In § 3.2, the stability of interface under the action of electric fields was discussed. The instability was quantified by the structure height difference between the rising and the falling tips. One key issue is the interfacial morphology of the RTI, which is the subject of this section. The interface exhibits various morphology patterns even with the same structure height. It is reasonable to conjecture that the electric field orientation and strength may play important roles in determining the evolution of the interfacial morphology. Here attention is focused on two aspects of the interfacial morphology, with one concerning the width of the ‘spike’ and/or the ‘bubble’, and the other the appearance of the roll-ups at the tip. As in the above, the influence of the horizontal and vertical electric field on the interfacial morphology will be discussed in separate sections below.

3.3.1. Interfacial morphology under the action of horizontal electric field

Some representative results of the interfacial morphology and flow field in the presence of horizontal electric fields are shown in figure 8. Specifically, figure 8(a) shows the evolution of the interfacial morphology and flow fields for $E_b = 0.1$, which is a relative small value. Initially, the flow is characterized by a relatively simple pattern, with the heavy fluid falling down at the centre and the light fluid rising up at the two sides. As time progresses, the tail forms around the ‘spike’ and the vertex starts to emerge. The interface evolves into an even more complex pattern as time continues. With an increase in field strength, as shown in figure 8(b) for the case of $E_b = 0.2$, the ‘spike’ is shorter and thinner compared with figure 8(a). The suppressing effect of a horizontal electric field on the RTI illustrated here can be explained by the same mechanism as discussed above. With a stronger field, the instability is weakened by the electrical force along the interface, and only a small part wedges into the light fluid to form a shorter and thinner ‘spike’. Comparison of figure 8(a) and (b) shows that the similar flow field is obtained except that the falling part is smaller with a stronger electric field. An even stronger electric field ($E_b = 1.0$)

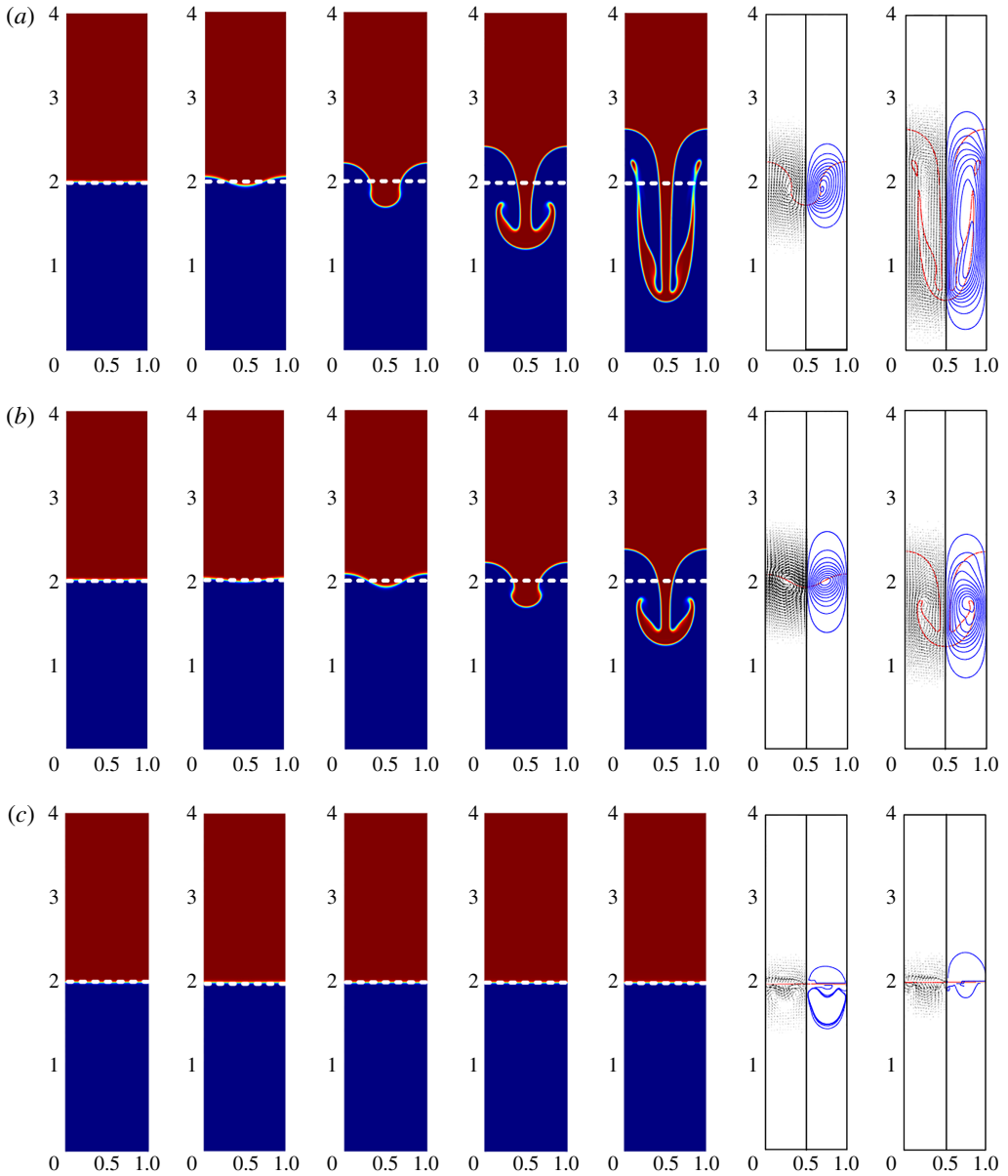


FIGURE 8. (Colour online) The RTI under the action of different horizontal electric fields: (a) $E_b = 0.1$, (b) $E_b = 0.2$ and (c) $E_b = 1.0$. Other parameters are the same as in table 1. The dimensionless time for the panels, from left to right, are $t^* = 0, 2.0, 3.0, 4.0$ and 5.0 . The dashed line represents the equilibrium interface. The vector flow field and streamline contours are plotted at right for $t^* = 3.0$ and $t^* = 5.0$.

can completely suppress the instability, which is shown in figure 8(c). For this case, the interface undergoes an oscillation with a rather small amplitude and eventually becomes essentially flat.

Appearance of fluid roll-ups is a common phenomenon associated with the RTI. The essential feature of the roll-up phenomenon is preserved for a weak electric

field. This is clearly shown in figure 8(a) where two counter-rotating vortices are formed along the sides of the falling fluid stream. Similar results in the absence of electric fields were observed by other researchers (Tryggvason 1988; He *et al.* 1999; Guermond & Quartapelle 2000; Ding *et al.* 2007). It is generally accepted that the roll-ups and vortices are caused by the secondary instability occurring at the interface between two fluids in motion (Daly 1967). The secondary instability appearing along the side of the ‘spike’ causes the interface to ‘mushroom’, which increases the effect of traction on the ‘spike’ and as a result vortex forms (Sharp 1984). For inviscid fluids, this secondary instability is often referred as the Kelvin–Helmholtz instability (KHI). For two viscous fluids with different viscosities, the Yih instability dominates the secondary instability (Yih 1967; Boomkamp & Miesen 1996). This study considers another explanation for the roll-ups. According to the Bjerknes theorem (Thorpe, Volkert & Ziemanski 2003), one source of the vorticity comes from the baroclinity, which is proportional to the cross-product of the density gradient and the pressure gradient, $\nabla p \times \nabla \rho$. In an RTI system, the gravity is the driving force in absence of electric field. The pressure tends to distribute vertically and its gradient ∇p points downward. At the two sides of the ‘spike’, $\nabla \rho$ is normal to the interface; namely, perpendicular to ∇p . Thus the vorticity generates at these spots and roll-ups occur under a persistent action of vorticity. It is worth noting that the Bjerknes theorem was proposed to explain the meteorological phenomena, in which the density and pressure change continuously. However, for a sharp interface system, the terms ∇p and $\nabla \rho$ are not well defined due to the jump of density and pressure across the interface. In the present paper, a diffuse interface model (i.e. phase field) is employed and the density varies continuously across the interface layer, for which the Bjerknes theorem is applicable.

The effect of permittivity ratio $\varepsilon_2/\varepsilon_1$ on the RTI was analysed in §3.2. A key conclusion reached there is that the structure height of the RTI is almost identical for both $\varepsilon_2/\varepsilon_1 = 3:1$ and $\varepsilon_2/\varepsilon_1 = 1:3$ (see figures 4 and 6). Here, the influence of permittivity ratio on interfacial morphology is assessed. Figure 9 compares the shapes of the fluid–fluid interface at dimensionless time $t^* = 5.0$ for the cases of $\varepsilon_2/\varepsilon_1 = 3:1$ and $\varepsilon_2/\varepsilon_1 = 1:3$. As is evident in the figure, the falling ‘spikes’, albeit being the same in structure height, differ dramatically in detailed morphology. The ‘spike’ is very narrow for $\varepsilon_2/\varepsilon_1 = 3:1$, but much broader for the other case. The difference in the characteristics of roll-ups for the two cases is also rather remarkable. Apparently, the difference is caused by strong nonlinear interactions present in the system.

For these two cases, other parameters such as density and viscosity are kept the same; only the electrical permittivity ratio of the two fluids is inverted. To gain further insight into the behaviour shown in figure 9, the electrical force along the interface is plotted in figure 10 for different amplitudes of deformation. In figure 10(a), a set of curves are shown representing the two fluid interfaces at different times of evolution. Although the interfaces of the two cases (i.e. $\varepsilon_2/\varepsilon_1 = 3:1$ and $\varepsilon_2/\varepsilon_1 = 1:3$) evolve differently and neither follows the cosine functions, the use of the same interfaces would allow us to identify the difference in the characteristics of the electrical force distribution along the interface for these two cases, which in turn would shed light on the physics governing the development of the interface morphology under the action of the electric field. The force in the y direction determines the vertical motion of the interface and is plotted in figure 10(b,c). Similar force distribution can be obtained analytically (see appendix C). As stated before, the characteristics of the electric force and its action are important in determining the interfacial morphology. For an RTI system, the total electrical force is balanced by the hydrostatic pressure, and the non-uniform local force is a culprit for the interface deformation. More specifically, a

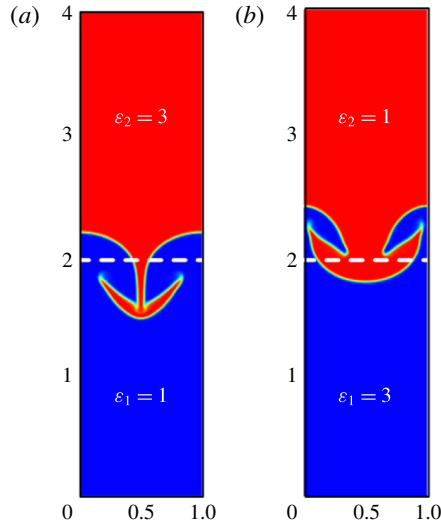


FIGURE 9. (Colour online) Comparison of interfacial morphologies of the RTI at dimensionless time $t^* = 5.0$ under the action of a horizontal electric field ($E_b = 0.3$) when the electrical permittivity ratios of two fluids are inverted: (a) $\varepsilon_2/\varepsilon_1 = 3 : 1$ and (b) $\varepsilon_2/\varepsilon_1 = 1 : 3$.

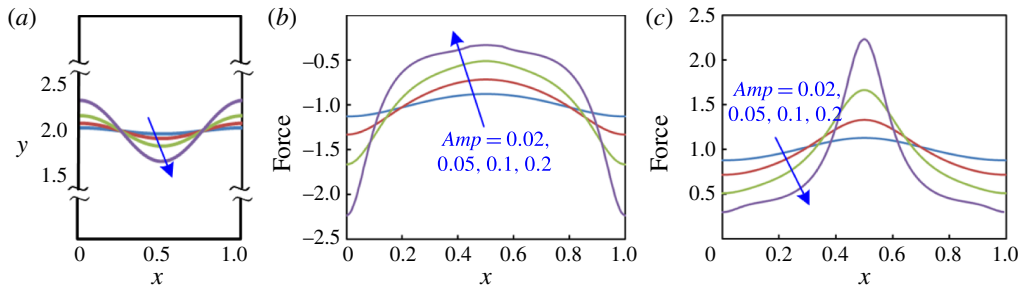


FIGURE 10. (Colour online) Distribution of the electrical force in the y direction along the interface as a function of horizontal electric fields: (a) interface shapes represented by a cosine wave function with different amplitudes $Amp = 0.02, 0.05, 0.1$ and 0.2 , the normalized electrical force in y direction along each of interface shapes displayed in (a) for $\varepsilon_2/\varepsilon_1 = 3 : 1$ (b), and for $\varepsilon_2/\varepsilon_1 = 1 : 3$ (c).

larger force in the y direction causes the interface to rise up, while a smaller one causes it to fall down, to satisfy the constraint of mass conservation. Inspection of figure 10 shows that, for a small deformation, the electrical force distribution nearly follows a cosine function, which means that half the interface ($0.25 < x < 0.75$) falls downward and the other half goes upward. This is also predicted by the linear analysis (see appendix A). For large deformations, nonlinear effects come into play and the distribution of electrical force along a cosine-shaped interface no longer follows a cosine function. Moreover, the force distributions differ more significantly in shape for the two cases as deformation becomes more severe, implying that in the nonlinear regime, the instability evolves differently for these two cases.

Let us now turn to the mechanism by which the electrical force affects the interfacial morphology. For that, it might be favourable to refer some previous analyses on the morphology of the classical RTI. According to Daly (1967), the traction plays a significant role in determining the interfacial morphology. During the RTI process, the traction exerted on the fluid is proportional to the density of the medium through which it moves, and hence the ‘spike’ always goes faster than the ‘bubble’. Total mass is required to be conserved, resulting in the ‘spike’ being longer and thinner than the ‘bubble’. With an electric field imposed, the electrical force along the interface modifies the effect of the traction, thereby causing a change of the interfacial morphology. For $\varepsilon_2/\varepsilon_1 = 3 : 1$, the electrical force is negative (i.e. pointing downward). The force is large in magnitude at the ‘bubble’, indicating an enforcement of the traction on the ‘bubble’. Thus the rising speed of the ‘bubble’ is slowed down, leading to a fat ‘bubble’ and a thin ‘spike’ (see figure 9a). On the contrary, for the case of $\varepsilon_2/\varepsilon_1 = 1 : 3$, the electrical force is positive and attains the maximum at the ‘spike’. Thus, the traction on the ‘spike’ is enforced, resulting in a fatter ‘spike’, as shown in figure 9(b).

3.3.2. Interfacial morphology under the action of vertical electric field

Simulations were also conducted to understand the influence of a vertical electric field on the development of the interfacial morphology. Figure 11 shows the evolution of the interface under the action of a vertical electric field (without gravity). The heavy fluid falls downward, forming a narrow needle-shaped ‘spike’ and the light fluid rises upward, forming a big ‘bubble’. From the flow field, one can see that the fluids simply fall and rise with no ‘tail’ formed during the process. The morphology is characterized by two noticeable features: no roll-ups and a long narrow ‘spike’. Thus, the vertical electric field produces a disturbing effect similar with gravity, causing the RTI to grow, but also differs from gravity in that no roll-ups will occur with a vertical electric field acting alone. A similar shape was reported by other researchers when a heavy fluid falls into another fluid with negligible density (i.e. $A = 1$) under gravity but in the absence of an electric field (Tryggvason 1988; Kull 1991). As stated before, the traction imposed on one fluid is proportional to the density of the medium fluid that it moves into (Daly 1967), and thus the traction on the ‘spike’ can be ignored when $A = 1$. Thus the ‘spike’ goes downward rapidly and renders itself a long and thin shape. Also, the presence of the roll-ups is attributed to the baroclinity along the ‘spike’. When $A = 1$, the heavy fluid flows into a vacuum. The pressure along the interface is approximately constant; as a result the pressure gradient is perpendicular to the interface. Apparently, the density gradient is always normal to the interface. Consequently $\nabla p \times \nabla \rho = 0$ or the baroclinity is zero with $A = 1$ and vorticity is not generated, whereby roll-ups do not form. As shown below, under action of a vertical field along, such a similar interfacial morphology forms in a vertical electric field due to the action of electrical force, the detailed mechanism would be revealed later.

The RTI driven by a combined action of a vertical electric field and gravity is illustrated in figure 12. As a comparison, the classical RTI with gravity alone ($E_b = 0$) is shown in figure 12(a). Comparison of the results reveals the different disturbing effects associated with the vertical field and the gravity: the roll-ups are absent in figure 11 when the field is present without gravity, whereas they show up in figure 12(a) when gravity is present without the electric field. Clearly, both gravity and the vertical electric field each aggravate the instability but produce different interfacial morphologies. This difference in nonlinear behaviour associated with gravity and a vertical field is manifest by the nature of the forces. Gravitational

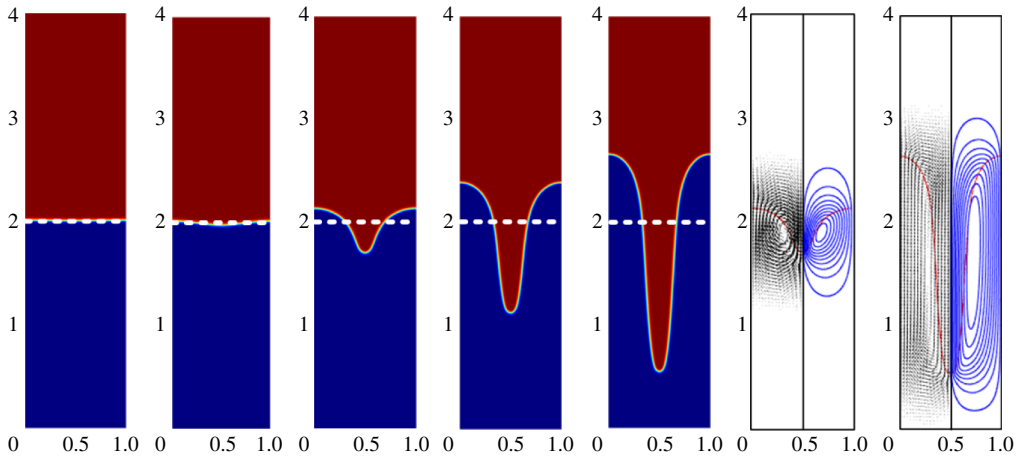


FIGURE 11. (Colour online) Time snapshot of interfacial morphology at $t^* = 0, 3.0, 6.0, 9.0$ and 12.0 (from left to right) and of the fluid flow field at $t^* = 6.0$ and 12.0 in the presence of a vertical electric field $E_b = 0.1$. The gravity is ignored and other parameters are listed in table 1.

force leads to non-zero baroclinity ($\nabla p \times \nabla \rho \neq 0$), which produces the vorticity and then causes the roll-ups at the two sides of the ‘spike’. For a vertical electric field without gravity, the electrical force acts normal to the fluid/fluid interface. This means that the pressure gradient is perpendicular to the interface and is aligned with the direction of density gradient, resulting in $\nabla p \times \nabla \rho = 0$. Thus, by the Bjerknes theorem (Thorpe *et al.* 2003), vorticity will not be baroclinically deposited along the interface. Consequently, the roll-ups will not form under the action of the vertical electric field. Figure 12(b,c) show the interfacial morphology in the presence of both gravity and the vertical electric field. Apparently, these interfacial morphologies are similar with figure 12(a) except that the heavy fluid falls more deeply with more complex vortex structure, suggesting that the vertical electric field intensifies the RTI. However, the secondary instability is not aggravated by the vertical field; as a matter of fact the width of the ‘spike’ is well controlled with a vertical field present. For different electric field strengths, the flow field and streamlines are similar, except that the flow pattern is elongated in the vertical direction for a stronger electric field, as shown in the accompanying fluid flow fields in figure 12. Furthermore, the roll-up structure remains approximately the same with different field strengths, indicating that vorticity deposited along the interface is caused primarily by the gravitational force.

The morphology shown in figure 12 corresponds to the case $\varepsilon_2/\varepsilon_1 = 3 : 1$. For a different permittivity ratio, the interfacial morphology is expected to be different. Figure 13 compares the interfacial morphology for different permittivity ratios for the same electrical strength. With $\varepsilon_2/\varepsilon_1 = 3 : 1$, the ‘spike’ is rather thin, whereas a broad ‘spike’ is obtained with $\varepsilon_2/\varepsilon_1 = 1 : 3$. Roll-ups are not obvious in both cases by the reason stated above. For the two cases, the vertical electrical force distribution along the interface is plotted in figure 14 assuming the interface takes a shape of cosine function. When the interface deformation is small, the force distribution follows the cosine wave function, whereas a large deformation distorts the distribution of electrical force, manifesting the nonlinear behaviour. Similar results are obtained by the analytical method (see appendix C). For $\varepsilon_2/\varepsilon_1 = 3 : 1$, the electrical force points

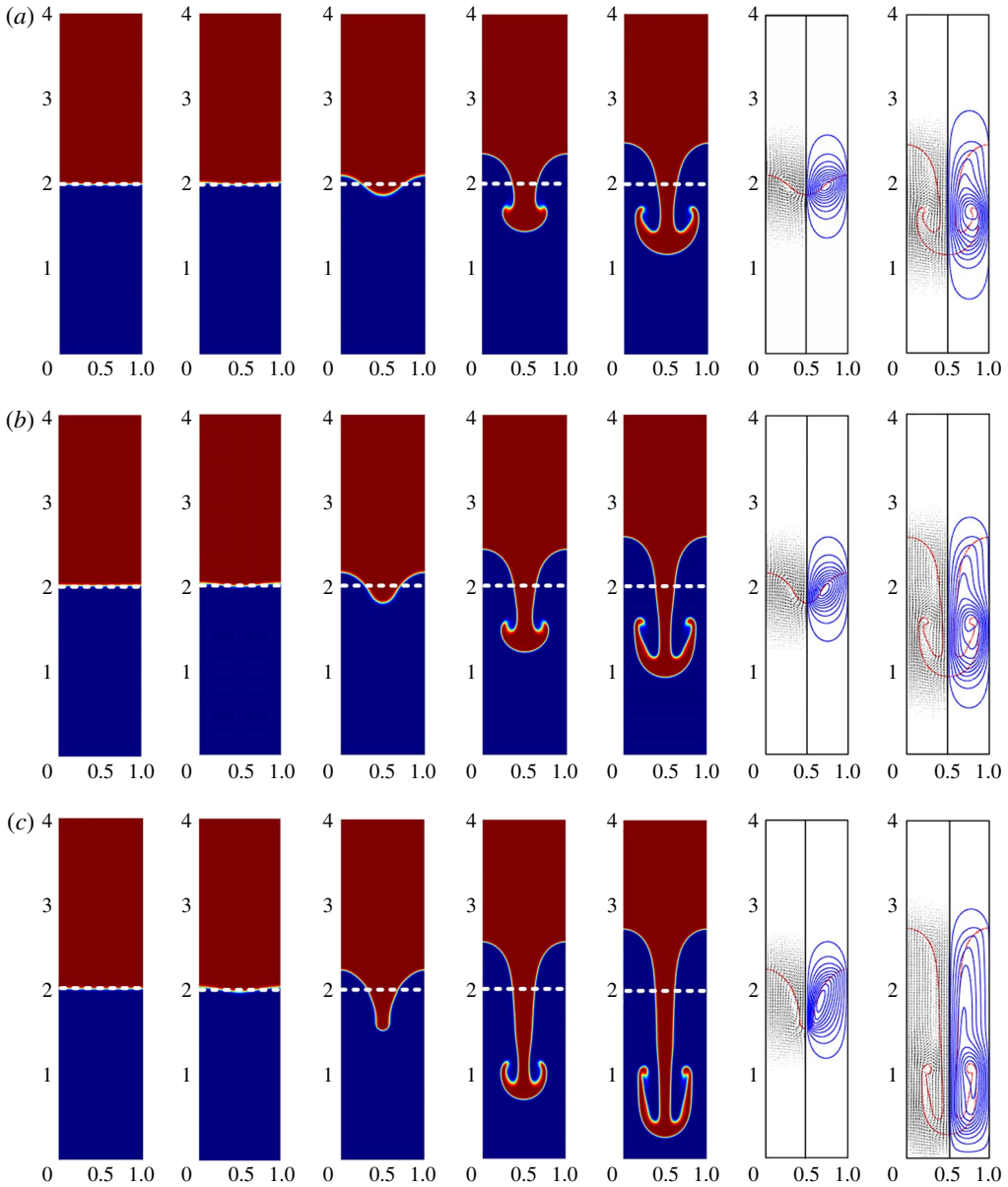


FIGURE 12. (Colour online) Evolution of the interfacial morphology under the action of vertical electric fields: (a) $E_b = 0$, (b) $E_b = 0.1$ and (c) $E_b = 0.3$. Other parameters are given in table 1. The dimensionless time for the subfigures, from left to right, are $t^* = 0, 1.0, 2.0, 3.0$ and 3.5 for interface evolution and $t^* = 2.0$ and 3.5 for the flow fields.

downward and attains a maximum in magnitude at the ‘spike’. This electrical force counterbalances the traction on the ‘spike’, driving the ‘spike’ to evolve fast and deform into a narrow shape. On the other hand, for $\varepsilon_2/\varepsilon_1 = 1:3$, the electrical force points upwards and is strongest at the ‘bubble’. Thus the ‘bubble’ rises higher and is thin, again because the traction at the ‘bubble’ is counterbalanced by the electric force.

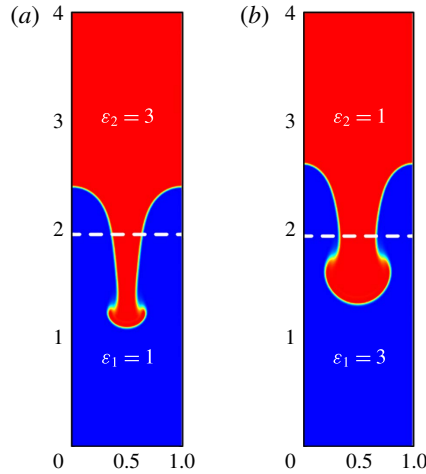


FIGURE 13. (Colour online) The effect of the electrical permittivity ratio on the interfacial morphology with a vertical electric field of $E_b = 0.5$ at dimensionless time $t^* = 1.5$: (a) $\varepsilon_2/\varepsilon_1 = 3 : 1$ and (b) $\varepsilon_2/\varepsilon_1 = 1 : 3$.

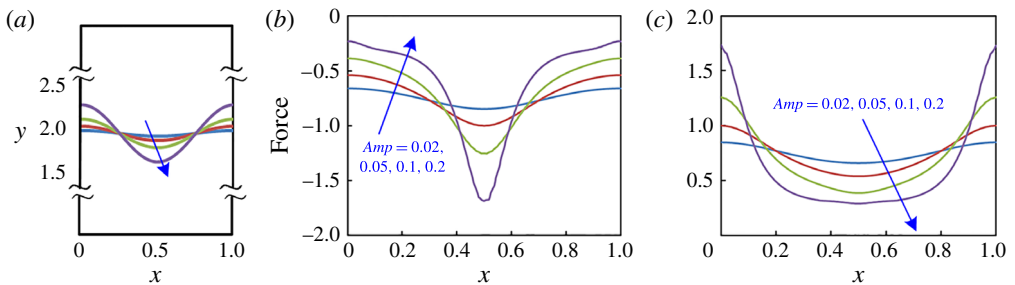


FIGURE 14. (Colour online) Distribution of the y component of the electric force along the interface with the presence of different vertical electric fields: (a) interface shapes represented by a cosine function with different amplitudes: $Amp = 0.02, 0.05, 0.1$ and 0.2 , and normalized electrical force in y direction along the interface for $\varepsilon_2/\varepsilon_1 = 3 : 1$ (b) and for $\varepsilon_2/\varepsilon_1 = 1 : 3$ (c).

3.4. Influence of the viscosity

The influence of viscosity is considered in this section. Figure 15(a) shows the effect of the Reynolds number on the RTI for a given horizontal electric field. As depicted in the figure, for fluids with a large viscosity (i.e. a small Reynolds number) the interface gradually returns to the equilibrium state (flat interface) and no interface oscillation is observed, that is, the system is overdamped. For fluids with a small viscosity, on other hand, the interface takes a damped oscillation (see the curves of $Re = 20, 50, 100, 1000$). If the fluids are inviscid, no convergent results are obtained even with continuous grid refinement. As pointed by several authors (Tryggvason 1988; He *et al.* 1999), this is caused by an occurrence of numerical singularity on vortex sheet at the centre of the roll-up. From the trend shown in figure 15(a), it is reasonable to suggest that for inviscid fluids the perturbation takes the form of undamped oscillation; the same conclusion is also reached in appendix A. Figure 15(b) shows the RTI in

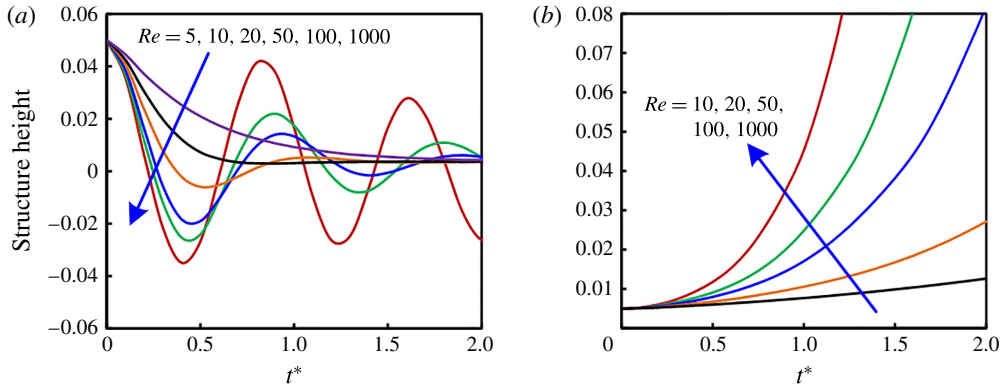


FIGURE 15. (Colour online) Effect of viscosity on the evolution of the interface structure height in (a) a horizontal electric field ($E_b = 4.0$) and (b) a vertical electric field ($E_b = 0.2$). The electrical permittivity ratio of the two fluids is $\epsilon_2/\epsilon_1 = 3 : 1$ and other parameters are given in table 1.

a vertical electric field as a function of viscosity; clearly the system in this case is always unstable. It is also noted that a large viscosity results in a slower evolution of structure height.

The nature of viscosity is to impede the fluid motion in shearing flows and hence the interface movement. Specifically, a large viscosity results in a slower interface movement. This is also evident in figure 15(a) by examining the slopes of the curves, which could be interpreted as the speed at which the interface moves at a given instant in time. The decay rate at which the perturbed interface eventually converges to its equilibrium state is an important issue which is affected by the viscosity of the fluid and the applied electric field. By comparing the curves of $Re = 20, 50, 100$ and 1000 , one may conclude that for such a system with oscillation, a large viscosity leads to a rapid decay rate. On the other hand, for the system without oscillation, a large viscosity leads to a slow decay rate (see the curves of $Re = 5$ and 10). The viscous force in this case is in a role of preventing the interface perturbation from retreating to the equilibrium. To sum up, the viscosity has different effects on the decay rates for over- and underdamped interface oscillations. This is also consistent with the analysis of viscous effects in appendix A.

3.5. Influence of the wavelength

In the computations presented above, one single mode perturbation with the fixed wavelength $\lambda = 1$ was taken. Here the influence of the wavelength on the RTI is considered and some computed results are presented in figure 16. It is apparent that the wavelength w dramatically affects the instability for both horizontal and vertical electric fields, which is supported by the results of the linear analysis in appendices (see figures 18 and 20). For a horizontal electric field ($E_b = 0.3$), figure 16(a) shows that the interface is stable for $\lambda = 0.5$ and unstable for $\lambda = 1$ and 2 . This result is consistent with the linear theory (see (A 1) in appendix A), which predicts the growth rate is $s = -14.8 \pm 191.9i$ (stable) for $\lambda = 0.5$, $s = 0.13$ (unstable) for $\lambda = 1$ and $s = 34.5$ (unstable) for $\lambda = 2$. In the case of the vertical field ($E_b = 0.1$), the structure evolves slower with increasing the wavelength, as shown in figure 16(b). According to the linear theory, a growth rate of $s = 73.4$ is predicted for $\lambda = 0.5$, $s = 54.8$ for $\lambda = 1$

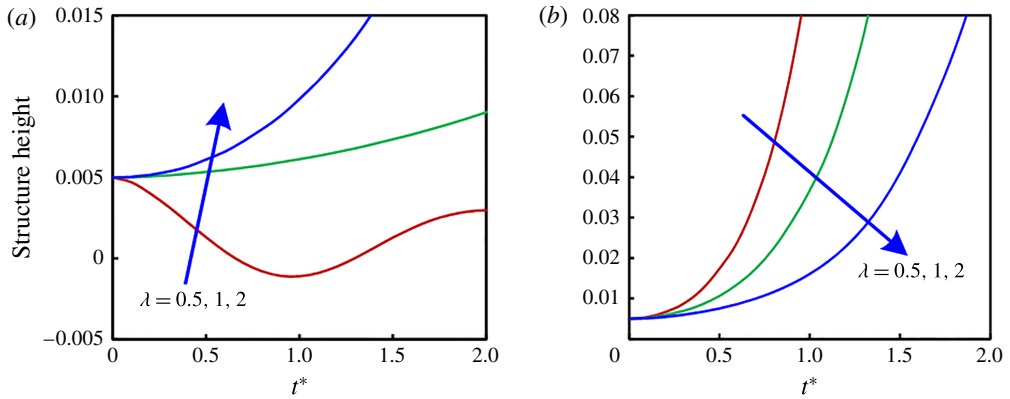


FIGURE 16. (Colour online) (a) The effect of wavelength on the RTI in a horizontal electric field $E_b = 0.3$; the wavelength λ is varied from 0.5, 1 to 2 and other parameters are as in table 1. (b) The effect of wavelength on the RTI in a vertical electric field $E_b = 0.1$.

and $s = 39.1$ for $\lambda = 2$. This agrees with the numerical results as the interface becomes less unstable for $\lambda = 2$ and more unstable for $\lambda = 0.5$. Although the instability depends on the wavelength, no significant effects of the wavelength on the development of interfacial morphology were observed.

3.6. Multiple mode

The single mode RTI is commonly used in numerical simulations, as it serves a base case for benchmark studies and has led to the discovery of many interesting phenomena. However, in reality the RTI tends to evolve from an initial random perturbation with multiple wavelengths. In this section, the effect of electric field on the RTI with a multiple mode perturbation is studied with the phase field numerical model presented above. For this, the computational domain of a square $[0, 4] \times [0, 4]$ is used with an initial perturbation of the fluid interface given by $y(x) = Amp \sum_{n=1}^N (a_n/2N) \cos(n\pi x/2) + (b_n/2N) \sin(n\pi x/2)$, where $Amp = 0.025$ is the amplitude and a total of 20 modes ($N = 20$) were used. The coefficients, a_n and b_n , are random numbers distributed between $[-1, 1]$ and for convenience, the initial interface henceforth is referenced to as a random perturbation. The boundary conditions at the two lateral sides for fluid flow are changed to periodic conditions. The Reynolds number, the Atwood number and other dimensionless parameters are chosen as given table 1. Computed results for the structure height evolution are given in figure 17 for the RTI in horizontal and vertical electric fields. As evident in figure 17(a), the RTI generated by the random perturbation is suppressed by a horizontal electric field, and this suppression effect becomes stronger with increasing electric field. On the other hand, figure 17(b) illustrates that a vertical electric field tends to aggravate the RTI. These observations consistent with the results obtained with one single mode perturbation, as expected.

According to the linear theory (see appendices A and B), for a given set of parameters there exists a most unstable wavelength at which the instability evolves fastest. In figure 17(c), the evolution of the interfacial morphology of the RTI in the absence of an electric field is displayed. Calculations started with the random

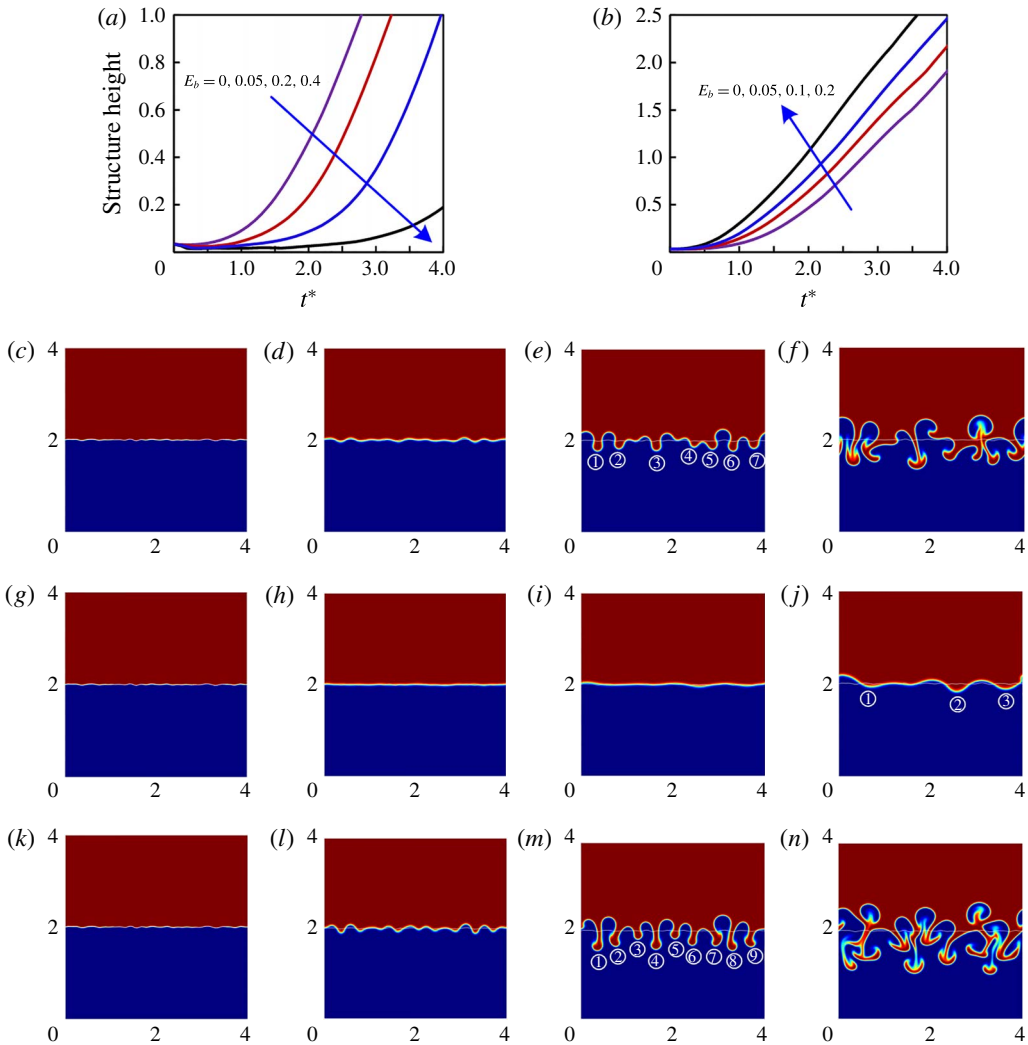


FIGURE 17. (Colour online) (a) Time development of the structure height in a horizontal electric field. (b) The structure height evolution in a vertical electric field. (c–e) Show the spatio-temporal evolution of the interfacial morphology for the classical RTI (electric field free), the RTI in a horizontal and in a vertical electric field. The electric field strength is $E_b = 0.2$ for (d) and $E_b = 0.1$ for (e).

perturbation imposed upon the interface at $t^* = 0$. The perturbation then is allowed to develop in time and evolves into a rather complicate structure eventually. At $t^* = 2.0$, the dominant wavelength becomes $4/7$ (i.e. seven periods are observed). This is consistent with the linear theory, which predicts that the most unstable wavelength is 0.68. This most unstable wavelength is altered by an electric field imposed. Specifically, a horizontal electric field increases the wavelength while a vertical one decreases it. Figure 17(d) shows the results for the RTI in a horizontal electric field $E_b = 0.2$. As can be seen, the instability evolves slowly for such a case. Only three periods of structure are obtained at $t^* = 3.0$, which indicates that the dominant wavelength is $4/3$. For a comparison, the most unstable wavelength is 1.92

according to the linear theory. On the other hand, when a vertical electric field is applied, the instability is amplified as indicated in figure 17(e). The wavelength of the structure is reduced by the imposed vertical electric field. Indeed, nine structures have appeared when $t^* = 2.0$. Once again, this is consistent with the linear analysis presented in appendix A.

4. Concluding remarks

A numerical phase field model has been developed for a nonlinear analysis of the RTI in the presence of an electric field. The model was validated against numerical results reported in literature and also the predictions by linear analysis. Numerical simulations were carried out to study the effect of the electric field on the stability and interfacial morphology, with focus on nonlinear effects. It is found that a horizontal electric field suppresses the RTI in both linear and nonlinear regimes. The instability is entirely suppressed if the applied horizontal field is sufficiently large. On the other hand, a vertical electric field has a destabilizing effect and aggravates the RTI. Moreover, in the absence of gravity, a vertical electric field only causes ‘spikes’ to form but not roll-ups for the cases studied. This is primarily because the force generated by the vertical field is perpendicular to the interface, and as such no vorticity along the interface can be generated baroclinically. Thus, the main destabilizing effect of a vertical field is to aggravate the ‘spike’ and does not contribute to the formation of roll-ups. The interfacial morphology is affected not only by the applied electric fields but also by the permittivity ratios of the fluids. If the upper denser fluid has a larger electrical permittivity, then a long and thin ‘spike’ forms. The ratio of permittivity being inversed (i.e. the two dielectric constants are interchanged), a short and wide ‘spike’ is obtained. This nonlinear behaviour is in contrast with linear analysis, which states that the instability is unchanged if the dielectric constants of the two fluids are interchanged.

Acknowledgements

This work was financed by China Postdoctoral Science Foundation (2015M570826), National Engineering Laboratory for Highway Maintenance Equipment (310825161103), National Instrumentation Program (no. 2013YQ190467) and Major Research Plan of NSFC on Nanomanufacturing (90923040). Q.Y. acknowledges the partial support of the University of Michigan-Dearborn as a visiting PhD student. F.X. acknowledges the partial support from NSFC (11372243), the Major International Joint Research Program of China (11120101002), and the International Science & Technology Cooperation Program of China (2013DFG02930). Helpful discussion with Professor D. Meiron of California Institute of Technology on the subject of Bjerknes theorem is also gratefully acknowledged. Useful comments from a reviewer are also gratefully appreciated.

Appendix A. Linear stability analysis on RTI in a horizontal electric field

In this section, the linear stability analysis of the RTI under the action of horizontal electric fields is considered. The electric field and fluid flow are sufficient to describe the system, and hence the phase field becomes trivial. For the configuration in figure 1, the governing equation for electric field is the Laplace equation, conservation of mass and momentum for fluid flows (Cimpeanu *et al.* 2014),

$$\nabla^2 V^{(i)} = 0, \quad (\text{A } 1)$$

$$\nabla \cdot \mathbf{u}^{(i)} = 0, \quad (\text{A } 2)$$

$$\rho(\mathbf{u}_t^{(i)} + \mathbf{u}^{(i)} \cdot \nabla \mathbf{u}^{(i)}) = -\nabla p^{(i)} + \mu_i \nabla^2 \mathbf{u}^{(i)} + \rho_i \mathbf{g}, \quad (\text{A } 3)$$

where $i = 1, 2$ represent fluid 1 and 2. The fluids are perfect dielectrics with constant permittivities; thus the electrical force are absent in each bulk fluid. The electrical force manifests itself at the fluid–fluid interface and thus affects its boundary condition.

Initially, the interface is flat and the fluids are quiescent. These base states can be written as (Melcher & Schwarz Jr 1968),

$$V^{(1)} = V^{(2)} = E_0x, \tag{A 4}$$

$$\mathbf{u}^{(1)} = \mathbf{u}^{(2)} = 0, \tag{A 5}$$

$$p^{(1)} = -\rho_1gy + (\rho_1 - \rho_2)gH_0, \quad p^{(2)} = -\rho_2gy - \frac{1}{2}\varepsilon_0(\varepsilon_2 - \varepsilon_1)E_0^2; \tag{A 6a,b}$$

$$f(x) = H_0. \tag{A 7}$$

In order to study the stability of the system, an infinitesimal perturbation is added to the base state, viz.

$$V^{(1)} = E_0x + \hat{V}^{(1)}(y)e^{st-jkx}, \quad V^{(2)} = E_0x + \hat{V}^{(2)}(y)e^{st-jkx}; \tag{A 8a,b}$$

$$\mathbf{u}^{(1)} = \hat{\mathbf{u}}^{(1)}(y)e^{st-jkx}, \quad \mathbf{u}^{(2)} = \hat{\mathbf{u}}^{(2)}(y)e^{st-jkx}; \tag{A 9a,b}$$

$$\left. \begin{aligned} p^{(1)} &= \hat{p}^{(1)}(y)e^{st-jkx} - \rho_1gy + (\rho_1 - \rho_2)gH_0, \\ p^{(2)} &= \hat{p}^{(2)}(y)e^{st-jkx} - \rho_2gy - \frac{1}{2}\varepsilon_0(\varepsilon_2 - \varepsilon_1)E_0^2; \end{aligned} \right\} \tag{A 10}$$

$$f = H_0 + \xi e^{st-jkx}, \tag{A 11}$$

where $k = 2\pi/\lambda$ (λ the wavelength) is the wavenumber.

The boundary conditions on the channel walls are no-slip conditions for the fluid flow and no vertical component of the electric field (Baranyk *et al.* 2012),

$$\partial V^{(1)}/\partial y = 0, \quad \mathbf{u}^{(1)} = 0 \quad \text{at } y = 0; \tag{A 12a,b}$$

$$\partial V^{(2)}/\partial y = 0, \quad \mathbf{u}^{(2)} = 0 \quad \text{at } y = l. \tag{A 13a,b}$$

At the interface $y = f(x) \approx H_0$, the field variables should satisfy the physical constraints given in terms of the kinematic conditions, the continuity of the normal component of the electric displacement, the continuity of tangential component of the electric field and the continuity of normal stress,

$$\mathbf{u}_y^{(1)} = \frac{\partial f}{\partial t} + \mathbf{u}_x^{(1)} \frac{\partial f}{\partial x}, \quad \mathbf{u}_y^{(2)} = \frac{\partial f}{\partial t} + \mathbf{u}_x^{(2)} \frac{\partial f}{\partial x}; \tag{A 14a,b}$$

$$\mathbf{n} \cdot (\varepsilon_1 \nabla V^{(1)}) = \mathbf{n} \cdot (\varepsilon_2 \nabla V^{(2)}), \quad \mathbf{t} \cdot \nabla V^{(1)} = \mathbf{t} \cdot \nabla V^{(2)}; \tag{A 15a,b}$$

$$\sigma_{ij}^{(1)} \cdot \mathbf{n} - \sigma_{ij}^{(2)} \cdot \mathbf{n} = \gamma (\nabla_s \cdot \mathbf{n}) \cdot \mathbf{n}, \tag{A 16}$$

where $\nabla_s = \nabla - \mathbf{n}(\mathbf{n} \cdot \nabla)$ is the surface divergence operator and $\sigma_{ij}^{(k)}$ is the stress of the fluid k ($k = 1$ for fluid 1 and $k = 2$ for fluid 2), expressed a sum of the hydrostatic pressure, surface tension stress and electrical stress tensor,

$$\sigma_{ij}^{(k)} = \left[\begin{array}{cc} -p^{(k)} + 2\mu^{(k)} \frac{\partial u^{(k)}}{\partial x} + \varepsilon_0 \varepsilon_k \left(\frac{1}{2} E_x^2 - \frac{1}{2} E_y^2 \right) & \mu^{(k)} \left(\frac{\partial u^{(k)}}{\partial y} + \frac{\partial v^{(k)}}{\partial x} \right) + \varepsilon_0 \varepsilon_k E_x E_y \\ \mu^{(k)} \left(\frac{\partial u^{(k)}}{\partial y} + \frac{\partial v^{(k)}}{\partial x} \right) + \varepsilon_0 \varepsilon_k E_x E_y & -p^{(k)} + 2\mu^{(k)} \frac{\partial v^{(k)}}{\partial y} + \varepsilon_0 \varepsilon_k \left(-\frac{1}{2} E_x^2 + \frac{1}{2} E_y^2 \right) \end{array} \right]. \tag{A 17}$$

The normal and tangential vector of the interface is given by the following expressions,

$$\mathbf{n} = \left(-\frac{\partial f}{\partial x}, 1 \right) / \sqrt{1 + \left(\frac{\partial f}{\partial x} \right)^2}, \quad \mathbf{t} = \left(1, \frac{\partial f}{\partial x} \right) / \sqrt{1 + \left(\frac{\partial f}{\partial x} \right)^2}. \quad (\text{A } 18a,b)$$

The governing equations can be solved along with boundary conditions for the given interface perturbations. The condition for a non-trivial solution leads to the following dispersion equation,

$$\begin{aligned} & \left[\frac{gk(\alpha_2 - \alpha_1)}{s^2} - \frac{k^3\gamma}{s^2(\rho_1 + \rho_2)} - C_3 - \frac{C_3 k^2 E_0^2 \varepsilon_0 (\varepsilon_2 - \varepsilon_1)^2}{s^2(\varepsilon_2 + \varepsilon_1)(\rho_1 + \rho_2)} \right] \\ & \times (C_1 q_2 \alpha_1 + C_2 q_1 \alpha_2 - k) - 4C_3 k \alpha_1 \alpha_2 \\ & + \frac{4C_3 k^2}{s} (\alpha_2 v_2 - \alpha_1 v_1) [C_1 q_2 \alpha_1 - C_2 q_1 \alpha_2 + C_3 k (\alpha_2 - \alpha_1)] \\ & + \frac{4C_3 k^3}{s^2} (\alpha_2 v_2 - \alpha_1 v_1)^2 (q_2 C_1 - k)(q_1 C_2 - k) = 0, \end{aligned} \quad (\text{A } 19)$$

where $q_1 = \sqrt{k^2 + s\rho_1/\mu_1}$, $q_2 = \sqrt{k^2 + s\rho_2/\mu_2}$, $C_1 = \tanh(kH_0) \coth(q_2 H_0)$, $C_2 = \tanh(kH_0) \coth(q_1 H_0)$, $C_3 = \coth(kH_0)$, $\alpha_1 = \rho_1/(\rho_1 + \rho_2)$ and $\alpha_2 = \rho_2/(\rho_1 + \rho_2)$. It is noted that for the above solution, use has been made of $l = 2H_0$.

Melcher & Schwarz Jr (1968) have studied the RTI in a horizontal electric field, and obtained the following dispersion equation,

$$\begin{aligned} & - \left[\frac{gk}{s^2} (\alpha_b - \alpha_a) + \frac{k^3 T}{s^2(\rho_a + \rho_b)} + 1 + \frac{k_x^2 E_0^2 \varepsilon_0 (\varepsilon_a - \varepsilon_b)^2}{s^2(\rho_a + \rho_b)(\varepsilon_a + \varepsilon_b)} \right] \\ & \times (q_b \alpha_a + q_a \alpha_b - k) - 4k \alpha_b \alpha_a + \frac{4k^2}{s} (\alpha_b v_b - \alpha_a v_a) [(\alpha_a q_b - \alpha_b q_a) + k(\alpha_b - \alpha_a)] \\ & + \frac{4k^3}{s^2} (\alpha_b v_b - \alpha_a v_a)^2 (q_b - k)(q_a - k) = 0, \end{aligned} \quad (\text{A } 20)$$

where T represents the surface tension coefficient. It is noted that in their original equation (Melcher & Schwarz Jr 1968, (35)), a sign '+' between the terms $(gk/s^2)(\alpha_b - \alpha_a)$ and $k^3 T/(s^2(\rho_a + \rho_b))$ was missing. Also, the above equation was obtained with the depth of the fluids set to infinity. The upper (bottom) fluid is referred as a (b), whereas in our case the upper (bottom) fluid is denoted by 2 (1). With $H_0 \rightarrow \infty$ (i.e. $C_1 = C_2 = C_3 = C_4 = 1$) substituted, our dispersion equation simplifies to the above equation given by Melcher and Schwarz.

In figure 18, the effect of horizontal electric field on the growth rate of the RTI is shown based on (A 19). To be consistent with the main text, the wavenumber k is normalized by L_c (L_c is the characteristic length). This holds true for all appendices below unless otherwise indicated. As can be seen, the growth rate is remarkably decreased with the presence of horizontal electric fields. For a perturbation with a specific wavenumber, the instability is completely suppressed when an electric field strong enough is applied. Also, the most dangerous wavenumber (i.e. the most unstable wavenumber) is shifted leftward as the electric field increases in strength. In figure 18, the wavenumber $k = 6.283$ corresponds to the perturbation that was used in the numerical model.

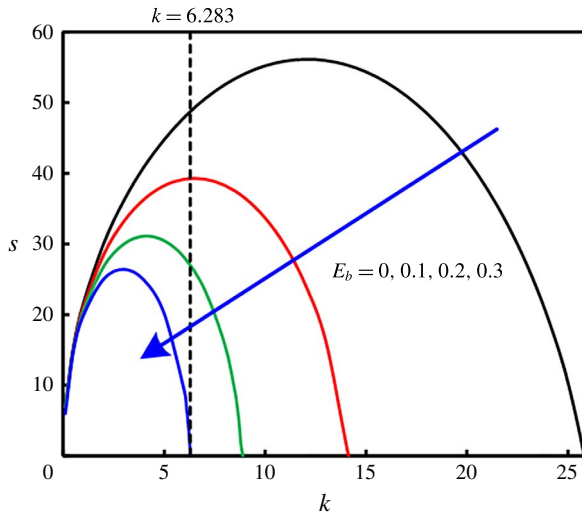


FIGURE 18. (Colour online) Linear growth rates as a function of horizontal electric fields characterized by electrical Weber number $E_b = \epsilon_0 \epsilon_m V_0^2 / (\rho_m g w^3)$; other parameters are the same as in table 1.

Equation (A 19) is used to study the effect of the viscosity on the RTI and results are shown in figure 19. In figure 19(a), all the curves pass through the critical point of $k_c = 3.187$. This state is achieved by a balance between the surface tension, electrical force and gravity and is thus independent of viscosity. For perturbations with $k < k_c$, the growth rate s is real and positive and the system is unstable, with the growth rate increasing with a decrease in viscosity. Similar curves exist for $E_b = 0$ but with $k_c = 25.822$. Thus, a horizontal field suppresses instability. In the region of $k > k_c$, the growth rate s is real but negative and thus the system is stable. However, there exists a turning point k_t at which the line of the real part of s changes its slope (see figure 19a). Similar points are also observed elsewhere (Chandrasekhar 1961). In figure 19(b), the $\text{Im}(s)$ is plotted as a function of viscosity. As it can be seen, the turning point marks the emergence of the imaginary part of s or $\text{Im}(s) > 0$ for $k > k_t$, and $\text{Im}(s) = 0$ for $k < k_t$. Moreover, k_t decreases with the fluid viscosity, with an inviscid fluid collapsing its turning point into the critical point (or $k_c = k_t$). Though the system is stable at $k > k_c$, the turning point differentiates the response of the fluid to the perturbation. In the region of $k_t > k > k_c$, the perturbed interface is overdamped and retreats directly to the plane equilibrium surface without oscillation (or $\text{Im}(s) = 0$). There, a large viscosity provides a strong resistance to the movement of the perturbed interface back to its equilibrium position and thus leads to a smaller $\text{Re}(s)$ value or a slow interface decay rate (see figure 19a). In the region of $k > k_t$, on the other hand, the interface goes through oscillations whose amplitude decays with time and eventually recedes to the equilibrium (i.e. flat surface), and a large viscosity gives rise to a high decaying rate. This is consistent with the numerical observation in figure 15, which used $k = 6.283$.

The turning point, k_t , is a solution to the characteristic equation (A 19). Mathematically, it is the point at which s changes from the real negative roots (only the less negative value of $\text{Re}(s)$ is plotted in figure 19) and becomes complex conjugate roots. Physically, it marks the point at which aperiodically damped modes ($k_c < k < k_t$)

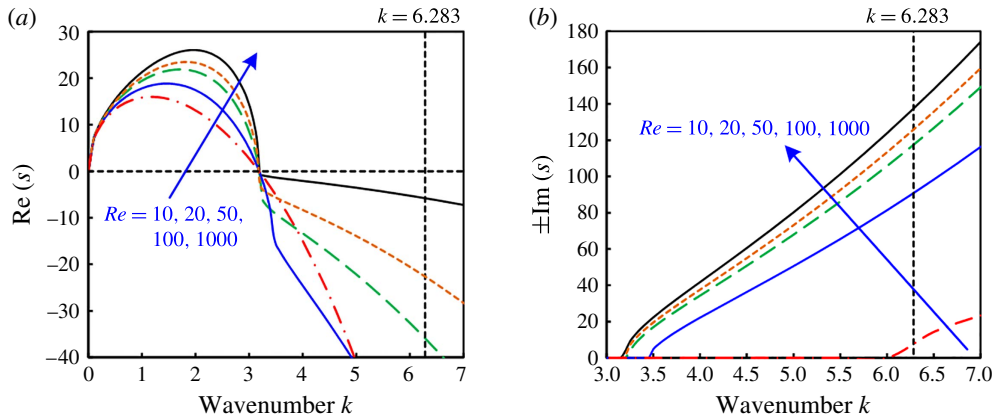


FIGURE 19. (Colour online) Growth rates as a function of the viscosity characterized by Reynolds number in a horizontal electric field: (a) the real part and (b) the imaginary part. The electrical Weber number $E_b = 4.0$ and other parameters are the same as in table 1.

changes to periodically damped modes ($k > k_t$). Figure 19 further indicates that the value of k_t is affected by a change of viscosity, and increases with an increase of viscosity, other parameters being fixed. Detailed analysis reveals that k_t represents a balance between the viscous damping effect and the effort of other forces (surface tension and electric force) responsible for oscillatory motion in the system for $k > k_c$. If viscous effect dominates, only aperiodically damped modes exist, which corresponds to the region $k_c < k < k_t$. For the case where viscous effect is comparable with the effect of the other forces, the interface undergoes an oscillatory motion of damped amplitude, which occurs for $k > k_t$. In the limiting case of inviscid fluid (or viscosity goes to zero), the interface undergoes an undamped periodic motion.

When $s \rightarrow 0$, (A 14) reduces to the condition for the marginal stability,

$$g(\alpha_2 - \alpha_1) - \frac{k^2\gamma}{(\rho_1 + \rho_2)} - \frac{\coth(kH_0)kE_0^2\epsilon_0(\epsilon_2 - \epsilon_1)^2}{(\epsilon_2 + \epsilon_1)(\rho_1 + \rho_2)} - 8k^3(\alpha_2 - \alpha_1)v_1v_2 \left(\frac{\alpha_2v_2 - \alpha_1v_1}{\alpha_1v_1 + \alpha_2v_2} \right) \coth(kH_0)[1 - \coth(kH_0)] = 0. \quad (\text{A } 21)$$

Substituting $k = 6.283$ and other parameters into (A 15), one obtains the critical value of the electrical Weber number, $E_b = 0.30$. It is interesting to note that the linear stability is unchanged if the dielectric constants of the two fluids are interchanged. This also holds true for a vertical electric field, as shown below.

Appendix B. Linear stability analysis of RTI in a vertical electric field

For the case of the RTI in the presence of a vertical electric field, the linear stability analysis is similar. The governing equations are the same as above. The base states are different and expressed as,

$$V^{(1)} = \frac{D_0}{\epsilon_1}y, \quad V^{(2)} = \frac{D_0}{\epsilon_2}y + \frac{(\epsilon_2 - \epsilon_1)V_0}{\epsilon_2 + \epsilon_1}; \quad (\text{B } 1a,b)$$

$$\mathbf{u}^{(1)} = \mathbf{u}^{(2)} = 0; \quad (\text{B } 2)$$

$$p^{(1)} = -\rho_1 g y + (\rho_1 - \rho_2) g H_0, \quad p^{(2)} = -\rho_2 g y - \frac{1}{2} \varepsilon_0 \left(\frac{1}{\varepsilon_1} - \frac{1}{\varepsilon_2} \right) D_0^2; \quad (\text{B } 3a,b)$$

$$f(x) = H_0, \quad (\text{B } 4)$$

where $D_0 = \varepsilon_1 \varepsilon_2 V_0 / (\varepsilon_1 + \varepsilon_2) H_0$. With an infinitesimal perturbation added to the base state, one has

$$V^{(1)} = \frac{D_0}{\varepsilon_1} y + \hat{V}^{(1)}(y) e^{st-jkx}, \quad V^{(2)} = \frac{D_0}{\varepsilon_2} y + \frac{(\varepsilon_2 - \varepsilon_1) V_0}{\varepsilon_2 + \varepsilon_1} + \hat{V}^{(2)}(y) e^{st-jkx}; \quad (\text{B } 5a,b)$$

$$\mathbf{u}^{(1)} = \hat{\mathbf{u}}^{(1)}(y) e^{st-jkx}, \quad \mathbf{u}^{(2)} = \hat{\mathbf{u}}^{(2)}(y) e^{st-jkx}; \quad (\text{B } 6a,b)$$

$$\left. \begin{aligned} p^{(1)} &= \hat{p}^{(1)}(y) e^{st-jkx} - \rho_1 g y + (\rho_1 - \rho_2) g H_0, \\ p^{(2)} &= \hat{p}^{(2)}(y) e^{st-jkx} - \rho_2 g y - \frac{1}{2} \varepsilon_0 \left(\frac{1}{\varepsilon_1} - \frac{1}{\varepsilon_2} \right) D_0^2; \end{aligned} \right\} \quad (\text{B } 7)$$

$$f = H_0 + \xi e^{st-jkx}, \quad (\text{B } 8)$$

where $k = 2\pi/\lambda$ (λ the wavelength) is the wavenumber.

The boundary conditions on the channel walls are no-slip conditions for the fluid flow and the Dirichlet conditions for the electric field,

$$V^{(1)} = 0, \quad \mathbf{u}^{(1)} = 0 \quad \text{at } y = 0; \quad (\text{B } 9a,b)$$

$$V^{(2)} = V_0, \quad \mathbf{u}^{(2)} = 0 \quad \text{at } y = l. \quad (\text{B } 10a,b)$$

The boundary conditions at the interface $y = f(x) \approx H_0$ are the same as above.

The condition for a non-trivial solution leads to a dispersion equation for a vertical electric field,

$$\begin{aligned} & \left[\frac{gk(\alpha_2 - \alpha_1)}{s^2} - \frac{k^3 \gamma}{s^2(\rho_1 + \rho_2)} - C_3 + \frac{C_3 k^2 D_0^2 \varepsilon_0 (\varepsilon_2 - \varepsilon_1)^2}{s^2 \varepsilon_1 \varepsilon_2 (\varepsilon_2 + \varepsilon_1) (\rho_1 + \rho_2)} \right] \\ & \times (C_1 q_2 \alpha_1 + C_2 q_1 \alpha_2 - k) - 4k \alpha_1 \alpha_2 \\ & + \frac{4C_3 k^2}{s} (\alpha_2 v_2 - \alpha_1 v_1) [C_1 q_2 \alpha_1 - C_2 q_1 \alpha_2 + k(\alpha_2 - \alpha_1)] \\ & + \frac{4C_3 k^3}{s^2} (\alpha_2 v_2 - \alpha_1 v_1)^2 (q_2 C_1 - k)(q_1 C_2 - k) = 0, \end{aligned} \quad (\text{B } 11)$$

where $q_1 = \sqrt{k^2 + s\rho_1/\mu_1}$, $q_2 = \sqrt{k^2 + s\rho_2/\mu_2}$, $C_1 = \tanh(kH_0) \coth(q_2 H_0)$, $C_2 = \tanh(kH_0) \coth(q_1 H_0)$, $C_3 = \coth(kH_0)$, $\alpha_1 = \rho_1/(\rho_1 + \rho_2)$ and $\alpha_2 = \rho_2/(\rho_1 + \rho_2)$. Again, $l = 2H_0$ was used. The growth rate of the RTI as a function of vertical electric fields is depicted in figure 20(a). Clearly, the growth rate is increased and the interface becomes more unstable in the presence of applied vertical fields. Figure 20(b) shows the effect of the viscosity on the RTI. If the wavenumber k is smaller than 60.97, then the system is unstable. For a small Reynolds number (i.e. a large viscosity), the growth rate of the perturbation decreases accordingly.

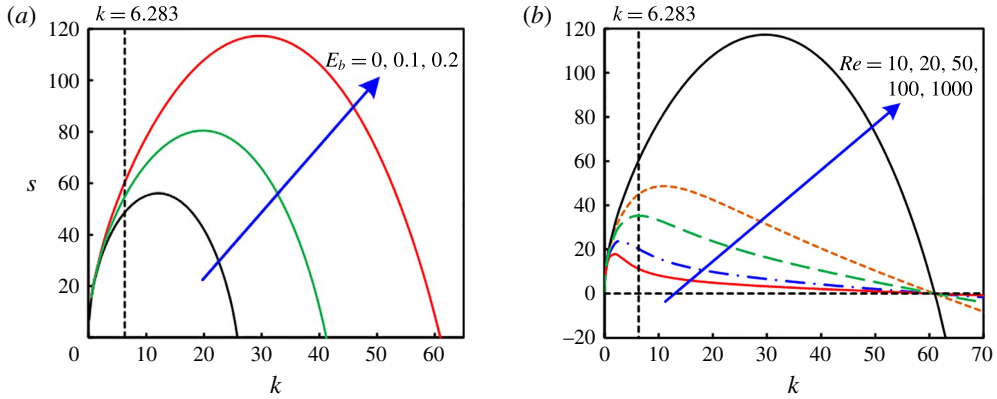


FIGURE 20. (Colour online) Growth rates as a function of (a) vertical electric fields characterized by electrical Weber number $E_b = \varepsilon_0 \varepsilon_m V_0^2 / (\rho_m g w l^2)$ with $Re = 1000$ and (b) the viscosity characterized by Reynolds number with $E_b = 0.4$. Other parameters are the same as in table 1.

Appendix C. Nonlinear analysis of the interfacial morphology

In figures 10 and 14, the electrical force and interfacial morphology are calculated by the numerical model. The force also can be obtained approximately by an analytical method. First, the instantaneous interface shape is assumed to be a first-order harmonic function. For this shape, electric potentials $V^{(1)}$ and $V^{(2)}$ are obtained in terms of a Fourier series, and the coefficients of the first few terms are determined by substituting the series into the governing equation along with associated boundary conditions. We then proceed to determine the electrical force along the interface. The detailed procedure is as follows.

The electric field is governed by the Laplace equation (i.e. (A 1)). For the RTI in a horizontal electric field, initially the fluid–fluid interface is flat. The base states of the interface and the electrical potential are written as (A 4) and (A 7), to which a small perturbation is added,

$$f(x) = H_0 + \xi e^{-jkx}; \tag{C 1}$$

$$V^{(1)} = E_0 x + \hat{V}_1^{(1)}(y) e^{-jkx} + \hat{V}_2^{(1)}(y) e^{-2jkx}; \tag{C 2}$$

$$V^{(2)} = E_0 x + \hat{V}_3^{(2)}(y) e^{-jkx} + \hat{V}_4^{(2)}(y) e^{-2jkx}, \tag{C 3}$$

representing the case with a deformed interface. Here, for an initial interface perturbation of ξe^{-jkx} , the second-order terms are retained for the electric potential. The reason for doing so is to determine how the nonlinearity of electric force comes into play for a first-order harmonic interface. For the electric potential $V^{(1)}$, one has the general solution $\hat{V}^{(1)}(y) = C_1 \cosh(ky) + C_2 \cosh(2ky)$ by substituting the expression of $V^{(1)}$ into the governing equation (A 1) and applying the boundary condition $\partial \hat{V}^{(1)}(y) / \partial y = 0$ at $y = 0$. By the same token, $\hat{V}^{(2)}(y) = C_3 \cosh[k(2H_0 - y)] + C_4 \cosh[2k(2H_0 - y)]$. The interface and the electrical potentials now become

$$f = H_0 + \xi e^{-jkx}; \tag{C 4}$$

$$V^{(1)} = E_0 x + C_1 \cosh(ky) e^{-jkx} + C_2 \cosh(2ky) e^{-2jkx}; \tag{C 5}$$

$$V^{(2)} = E_0 x + C_3 \cosh[k(2H_0 - y)] e^{-jkx} + C_4 \cosh[2k(2H_0 - y)] e^{-2jkx}. \tag{C 6}$$

Here quadratic terms are included to account for the nonlinear effect of the electric field. Now consider the following relations with $y = f(x) \approx H_0$,

$$\left. \begin{aligned}
 \cosh(ky) &= \cosh(kH_0 + k\hat{\xi}e^{-jkx}) \\
 &= \cosh(kH_0) \cosh(k\hat{\xi}e^{-jkx}) + \sinh(kH_0) \sinh(k\hat{\xi}e^{-jkx}) \\
 &\approx \cosh(kH_0) + \sinh(kH_0)k\hat{\xi}e^{-jkx}, \\
 \sinh(ky) &= \sinh(kH_0 + k\hat{\xi}e^{-jkx}) \\
 &= \sinh(kH_0) \cosh(k\hat{\xi}e^{-jkx}) + \cosh(kH_0) \sinh(k\hat{\xi}e^{-jkx}) \\
 &\approx \sinh(kH_0) + \cosh(kH_0)k\hat{\xi}e^{-jkx}, \\
 \cosh[k(2H_0 - y)] &= \cosh(kH_0 - k\hat{\xi}e^{-jkx}) \\
 &= \cosh(kH_0) \cosh(k\hat{\xi}e^{-jkx}) - \sinh(kH_0) \sinh(k\hat{\xi}e^{-jkx}) \\
 &\approx \cosh(kH_0) - \sinh(kH_0)k\hat{\xi}e^{-jkx}, \\
 \sinh[k(2H_0 - y)] &= \sinh(kH_0 - k\hat{\xi}e^{-jkx}) \\
 &= \sinh(kH_0) \cosh(k\hat{\xi}e^{-jkx}) - \cosh(kH_0) \sinh(k\hat{\xi}e^{-jkx}) \\
 &\approx \sinh(kH_0) - \cosh(kH_0)k\hat{\xi}e^{-jkx}.
 \end{aligned} \right\} \quad (C7)$$

At the interface, the normal component of electrical displacement and the tangential component of the electric field are continuous, see (A 15), where the normal and tangential vector of the perturbed interface is expressed as,

$$\left. \begin{aligned}
 \mathbf{n} &= (jk\hat{\xi}e^{-jkx}, 1) / \sqrt{1 - k^2\hat{\xi}^2e^{-2jkx}} \approx (jk\hat{\xi}e^{-jkx}, 1 + \frac{1}{2}k^2\hat{\xi}^2e^{-2jkx}), \\
 \mathbf{t} &= (1, -jk\hat{\xi}e^{-jkx}) / \sqrt{1 - k^2\hat{\xi}^2e^{-2jkx}} \approx (1 + \frac{1}{2}k^2\hat{\xi}^2e^{-2jkx}, -jk\hat{\xi}e^{-jkx}).
 \end{aligned} \right\} \quad (C8)$$

With ξ , $V^{(1)}$ and $V^{(2)}$ substituted into the boundary conditions, we have

$$\left. \begin{aligned}
 &-j\varepsilon_1 E_0 k \xi e^{-jkx} - C_1 \varepsilon_1 k^2 \cosh(kH_0) \xi e^{-2jkx} - C_1 \varepsilon_1 k^3 \sinh(kH_0) \xi^2 e^{-3jkx} \\
 &\quad - 2C_2 \varepsilon_1 k^2 \cosh(2kH_0) \xi e^{-3jkx} - 2C_2 \varepsilon_1 k^3 \sinh(2kH_0) \xi^2 e^{-4jkx} \\
 &\quad - C_1 \varepsilon_1 k \sinh(kH_0) e^{-jkx} - C_1 \varepsilon_1 k \cosh(kH_0) e^{-2jkx} \\
 &\quad - 2C_2 \varepsilon_1 k \sinh(2kH_0) e^{-2jkx} - 2C_2 \varepsilon_1 k^2 \cosh(2kH_0) \xi e^{-3jkx} \\
 &= -j\varepsilon_2 E_0 k \xi e^{-jkx} - C_3 \varepsilon_2 k^2 \cosh(kH_0) \xi e^{-2jkx} + C_3 \varepsilon_2 k^3 \sinh(kH_0) \xi^2 e^{-3jkx} \\
 &\quad - 2C_4 \varepsilon_2 k^2 \cosh(2kH_0) \xi e^{-3jkx} + 2C_4 \varepsilon_2 k^3 \sinh(2kH_0) \xi^2 e^{-4jkx} \\
 &\quad + C_3 \varepsilon_2 k \sinh(kH_0) e^{-jkx} - C_3 \varepsilon_2 k^2 \cosh(kH_0) \xi e^{-2jkx} \\
 &\quad + 2C_4 \varepsilon_2 k \sinh(2kH_0) e^{-2jkx} - 2C_4 \varepsilon_2 k^2 \cosh(2kH_0) \xi e^{-3jkx}, \\
 &-E_0 + C_1 j k \cosh(kH_0) e^{-jkx} + C_1 j k^2 \sinh(kH_0) \xi e^{-2jkx} + 2C_2 j k \cosh(2kH_0) e^{-2jkx} \\
 &\quad + 2C_2 j k^2 \sinh(2kH_0) \xi e^{-3jkx} + C_1 j k^2 \sinh(kH_0) \xi e^{-2jkx} + C_1 j k^3 \cosh(kH_0) \xi^2 e^{-3jkx} \\
 &\quad + 2C_2 j k^2 \sinh(2kH_0) \xi e^{-3jkx} + 2C_2 j k^3 \cosh(2kH_0) \xi^2 e^{-4jkx} \\
 &= -E_0 + C_3 j k \cosh(kH_0) e^{-jkx} - C_3 j k^2 \sinh(kH_0) \xi e^{-jkx} + 2C_4 j k \cosh(2kH_0) e^{-2jkx} \\
 &\quad - 2C_4 j k^2 \cosh(2kH_0) \xi e^{-3jkx} - C_3 j k^2 \sinh(kH_0) \xi e^{-2jkx} + C_3 j k^3 \cosh(kH_0) \xi^2 e^{-3jkx} \\
 &\quad - 2C_4 j k^2 \sinh(2kH_0) \xi e^{-3jkx} + 2C_4 j k^3 \cosh(2kH_0) \xi^2 e^{-4jkx}.
 \end{aligned} \right\} \quad (C9)$$

The perturbations are assumed to be small, $C_2 \ll C_1 \ll 1$, $C_4 \ll C_3 \ll 1$ and $\xi \ll 1$. Thus the following terms, $C_1 \xi^2$, $C_3 \xi^2$, $C_2 \xi$, $C_4 \xi$, $C_2 \xi^2$ or $C_4 \xi^2$ may be neglected. Then we let the terms with e^{-jkx} and e^{-2jkx} being identical on both sides,

$$\left. \begin{aligned} -j\varepsilon_1 E_0 k \xi - C_1 \varepsilon_1 k \sinh(kH_0) &= -j\varepsilon_2 E_0 k \xi + C_3 \varepsilon_2 k \sinh(kH_0), \\ C_1 \varepsilon_1 \cosh(kH_0) k \xi + C_2 \varepsilon_1 \sinh(2kH_0) &= C_3 \varepsilon_2 \cosh(kH_0) k \xi - C_4 \varepsilon_2 \sinh(2kH_0), \\ C_1 &= C_3, \\ C_2 \cosh(2kH_0) + C_1 k \sinh(kH_0) \xi &= C_4 \cosh(2kH_0) - C_3 k \sinh(kH_0) \xi, \end{aligned} \right\} \quad (C 10)$$

from which C_1 , C_2 , C_3 and C_4 are obtained,

$$\left. \begin{aligned} C_1 &= C_3 = \frac{j(\varepsilon_2 - \varepsilon_1) E_0 \xi}{(\varepsilon_1 + \varepsilon_2) \sinh(kH_0)}, \\ C_2 &= -\frac{j(\varepsilon_2 - \varepsilon_1) E_0 \xi^2 k}{(\varepsilon_1 + \varepsilon_2)^2} \left[\frac{(\varepsilon_2 - \varepsilon_1)}{\tanh(kH_0) \sinh(2kH_0)} + \frac{2\varepsilon_2}{\cosh(2kH_0)} \right], \\ C_4 &= -\frac{j(\varepsilon_2 - \varepsilon_1) E_0 \xi^2 k}{(\varepsilon_1 + \varepsilon_2)^2} \left[\frac{(\varepsilon_2 - \varepsilon_1)}{\tanh(kH_0) \sinh(2kH_0)} - \frac{2\varepsilon_1}{\cosh(2kH_0)} \right]. \end{aligned} \right\} \quad (C 11)$$

The electrical force applied at the interface is given by (Jackson 1999),

$$\mathbf{f}_e = \begin{bmatrix} f_x \\ f_y \end{bmatrix} = \begin{bmatrix} \left[\frac{1}{2} \varepsilon_0 \varepsilon (E_x^2 - E_y^2) n_x + \varepsilon_0 \varepsilon E_x E_y n_y \right]_2^1 \\ \left[\varepsilon_0 \varepsilon E_x E_y n_x + \frac{1}{2} \varepsilon_0 \varepsilon (-E_x^2 + E_y^2) n_y \right]_2^1 \end{bmatrix}, \quad (C 12)$$

where $[(\cdot)]_2^1 = (\cdot)_2 - (\cdot)_1$ denotes the jump in the quantity as the interface is crossed from the upper to the lower fluid. A quantity of main interest is the vertical component of electrical force f_y , as it determines the interfacial morphology,

$$f_y = [\varepsilon_0 \varepsilon E_x E_y n_x + \frac{1}{2} \varepsilon_0 \varepsilon (-E_x^2 + E_y^2) n_y]_2^1 \approx A_0 + A_1 \xi e^{-jkx} + A_2 \xi^2 e^{-2jkx}, \quad (C 13)$$

where

$$A_0 = -\frac{1}{2} \varepsilon_0 (\varepsilon_2 - \varepsilon_1) E_0^2; \quad (C 14)$$

$$A_1 = -\frac{\varepsilon_0 (\varepsilon_2 - \varepsilon_1)^2}{(\varepsilon_1 + \varepsilon_2)} \coth(kH_0) k E_0^2; \quad (C 15)$$

$$\begin{aligned} A_2 &= \frac{\varepsilon_0 (\varepsilon_2 - \varepsilon_1)}{4(\varepsilon_1 + \varepsilon_2)^2} \left\{ -7(\varepsilon_2 + \varepsilon_1)^2 + 2(\varepsilon_2 - \varepsilon_1)^2 \right. \\ &\quad \times [1 + \coth^2(kH_0) - 4 \coth(kH_0) \coth(2kH_0)] + 32\varepsilon_1 \varepsilon_2 \left. \right\} k^2 E_0^2. \end{aligned} \quad (C 16)$$

Here, up to quadratic terms are kept and other higher-order terms are truncated. The zeroth-order term (i.e. A_0) is dominant and determines the direction of electric force (i.e. pointing upwards or downwards). In linear perturbation analysis (see appendices A and B above), only the zeroth- and the first-order terms are considered. Here the second-order term (i.e. $A_2 \xi^2 e^{-2jkx}$) is retained to study the nonlinear effect of the electrical force.

The electrical force influences the interfacial morphology through (A 16) (i.e. boundary condition at the interface). In the expression of stress $\sigma_{ij}^{(k)}$, the hydrostatic

pressure $p^{(1)} = -\rho_1 g y + (\rho_1 - \rho_2) g H_0$, $p^{(2)} = -\rho_2 g y - (1/2)\epsilon_0(\epsilon_2 - \epsilon_1)E_0^2$. The above equation is essentially a force balance condition, where the total force includes hydrostatic force, electrical force, viscous force and surface tension force. Here we focus on the effect of electrical force on the interfacial morphology and, thus the viscous force is neglected for simplification. The electrical force causes the interfacial deformation, and the surface tension force increases to balance the electrical force. Ultimately a delicate balance is achieved to reach a steady state or equilibrium state. This steady state of the interfacial deformation is of the form, $y_s = H_0 + B_1 \xi e^{-jkx} + B_2 \xi^2 e^{-2jkx}$, and the force balance leads to the following expression,

$$f_y + (\rho_2 - \rho_1)g(y - H_0) + \frac{1}{2}\epsilon(\epsilon_2 - \epsilon_1)E_0^2 = -\gamma \frac{\partial^2 y_s / \partial x^2}{[1 + (\partial y_s / \partial x)^2]^{3/2}} \approx \gamma k^2 B_1 \xi e^{-jkx} + 4\gamma k^2 B_2 \xi^2 e^{-2jkx}. \tag{C 17}$$

Substituting f_y and y into the above equation, one has

$$B_1 = \frac{A_1 + (\rho_2 - \rho_1)g}{\gamma k^2}; \tag{C 18}$$

$$B_2 = \frac{A_2}{4\gamma k^2}. \tag{C 19}$$

For the two cases $\epsilon_2/\epsilon_1 = 3 : 1$ and $\epsilon_2/\epsilon_1 = 1 : 3$, the interfacial morphology differs from each other (see figure 9), for which the vertical components of the electrical force f_y are computed and depicted in figure 21. Clearly, with an increase of deformation (i.e. ξ), the nonlinear term $A_2 \xi^2 e^{-2jkx}$ comes into play. The obtained electrical force profile is similar to that in figure 10. Figure 21(c,d) correspond to the equilibrium interfacial deformation including the quadratic term for $\epsilon_2/\epsilon_1 = 3 : 1$ and $\epsilon_2/\epsilon_1 = 1 : 3$. Thus, a narrow falling spike is obtained for $\epsilon_2/\epsilon_1 = 3 : 1$ but a broad one for $\epsilon_2/\epsilon_1 = 1 : 3$; these observations are similar to those shown in figure 9.

We now proceed to the case of vertical field. The procedure is the same and the base state takes the form of (B 11) and (B 4). After adding the small perturbation to the base state, the interface and electrical potential become

$$f = H_0 + \xi e^{-jkx}; \tag{C 20}$$

$$V^{(1)} = \frac{D_0}{\epsilon_1} y + \hat{V}_1^{(1)}(y) e^{-jkx} + \hat{V}_2^{(1)}(y) e^{-2jkx}; \tag{C 21}$$

$$V^{(2)} = \frac{D_0}{\epsilon_2} y + \frac{(\epsilon_2 - \epsilon_1)V_0}{\epsilon_2 + \epsilon_1} + \hat{V}_1^{(2)}(y) e^{-jkx} + \hat{V}_2^{(2)}(y) e^{-2jkx}. \tag{C 22}$$

Substitution of $V^{(1)}$ into the governing equation (A 4) along with $\hat{V}^{(1)}(y) = 0$ at $y = 0$ yields $\hat{V}^{(1)}(y) = C_1 \sinh(ky) + C_2 \sinh(2ky)$. By the same procedure, $\hat{V}^{(2)}(y) = C_3 \sinh[k(2H_0 - y)] + C_4 \sinh[2k(2H_0 - y)]$. Thus, we have

$$f = H_0 + \xi e^{-jkx}; \tag{C 23}$$

$$V^{(1)} = \frac{D_0}{\epsilon_1} y + C_1 \sinh(ky) e^{-jkx} + C_2 \sinh(2ky) e^{-2jkx}; \tag{C 24}$$

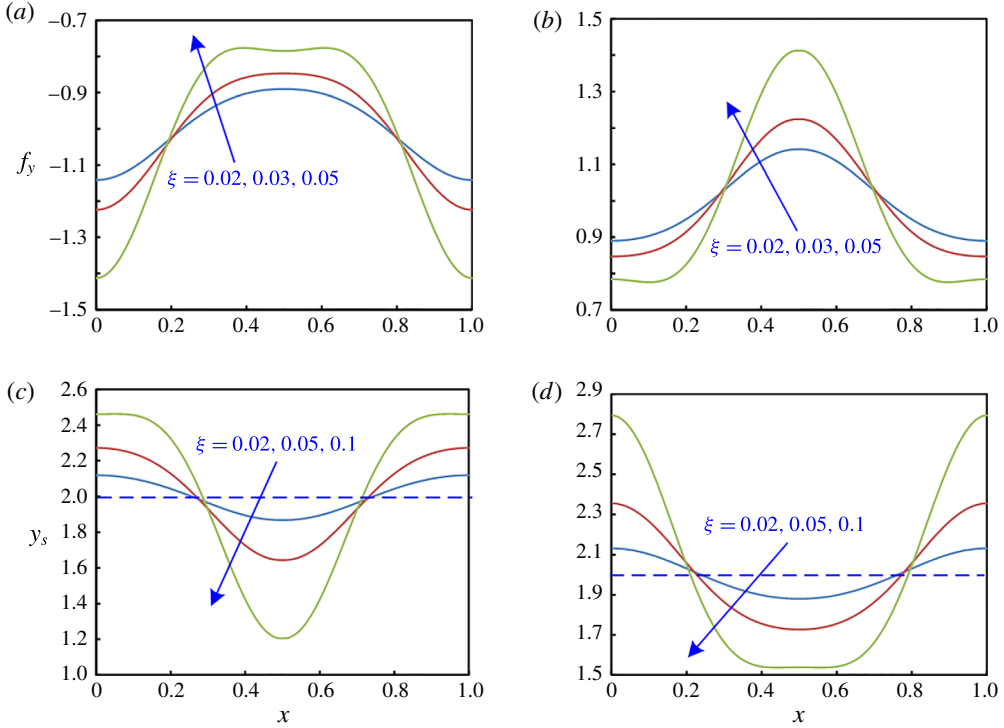


FIGURE 21. (Colour online) The vertical electrical force along the interface in a horizontal electric field. (a) $\epsilon_2/\epsilon_1 = 3 : 1$ and (b) $\epsilon_2/\epsilon_1 = 1 : 3$. The equilibrium deformation under the action of electrical force, with $E_b = 0.2$ and $We = 0.001$: (c) $\epsilon_2/\epsilon_1 = 3 : 1$ and (d) $\epsilon_2/\epsilon_1 = 1 : 3$. The position of x , ξ and y_s are normalized by L_c and electrical force by $\epsilon_0|\epsilon_2 - \epsilon_1|V_0^2/(2w^2)$.

$$V^{(2)} = \frac{D_0}{\epsilon_2}y + \frac{(\epsilon_2 - \epsilon_1)V_0}{\epsilon_2 + \epsilon_1} + C_3 \sinh[k(2H_0 - y)]e^{-jkx} + C_4 \sinh[2k(2H_0 - y)]e^{-2jkx}. \tag{C 25}$$

The same boundary conditions should be satisfied at the interface, i.e. the continuity of normal component of the displacement and continuity of the tangential component of the electric field, whence one has

$$\left. \begin{aligned} C_1 &= -\frac{(\epsilon_2 - \epsilon_1)D_0\xi}{\epsilon_1(\epsilon_2 + \epsilon_1) \sinh(kH_0)}, \\ C_2 &= \frac{(\epsilon_2 - \epsilon_1)D_0\xi^2k}{\epsilon_1(\epsilon_2 + \epsilon_1)^2} \left[\frac{(\epsilon_2 - \epsilon_1)}{\tanh(kH_0) \sinh(2kH_0)} + \frac{2\epsilon_1}{\cosh(2kH_0)} \right], \\ C_3 &= \frac{(\epsilon_2 - \epsilon_1)D_0\xi}{\epsilon_2(\epsilon_2 + \epsilon_1) \sinh(kH_0)}, \\ C_4 &= \frac{(\epsilon_2 - \epsilon_1)D_0\xi^2k}{\epsilon_2(\epsilon_2 + \epsilon_1)^2} \left[-\frac{(\epsilon_2 - \epsilon_1)}{\tanh(kH_0) \sinh(2kH_0)} + \frac{2\epsilon_2}{\cosh(2kH_0)} \right]. \end{aligned} \right\} \tag{C 26}$$

The electrical force in the vertical direction now takes the form of

$$f_y = [\epsilon_0\epsilon_x e_x n_x + \frac{1}{2}\epsilon_0\epsilon(-e_x^2 + e_y^2)n_y]_2^1 \approx A_0^* + A_1^*\xi e^{-jkx} + A_2^*\xi^2 e^{-2jkx}, \tag{C 27}$$

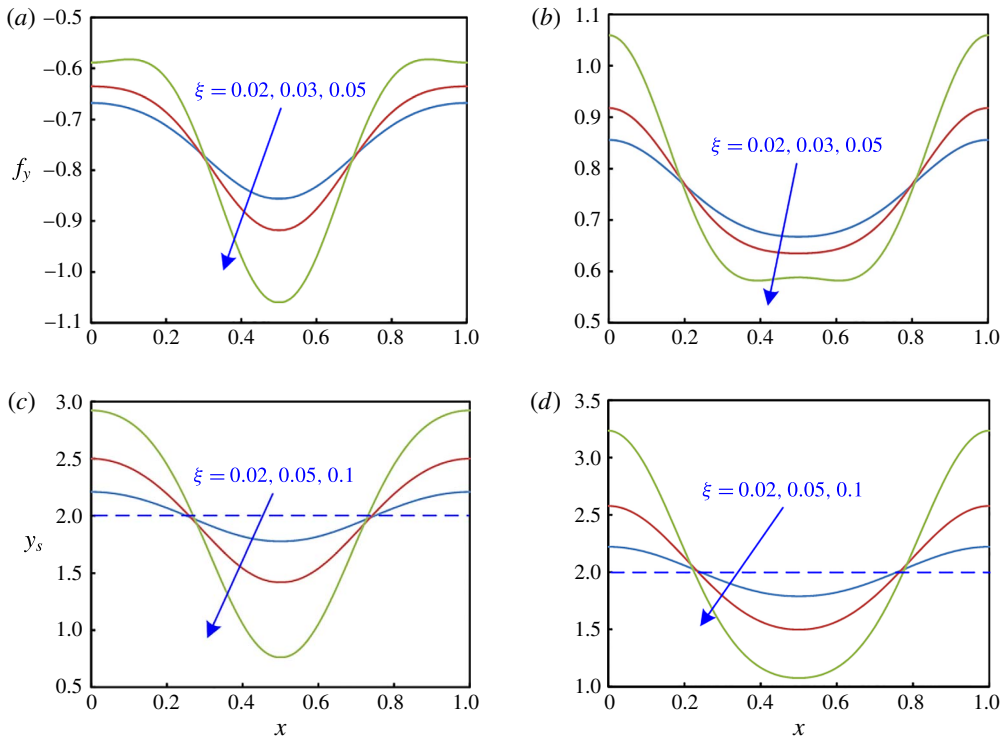


FIGURE 22. (Colour online) The vertical component of the electrical force in a vertical electric field. (a) $\varepsilon_2/\varepsilon_1 = 3 : 1$ and (b) $\varepsilon_2/\varepsilon_1 = 1 : 3$. The corresponding equilibrium deformation for (c) $\varepsilon_2/\varepsilon_1 = 3 : 1$ and (d) $\varepsilon_2/\varepsilon_1 = 1 : 3$ with $E_b = 5.0$ and $We = 0.02$. The position of x , ξ and y_s are normalized by L_c and electrical force by $\varepsilon_0|\varepsilon_2 - \varepsilon_1|V_0^2/(2l^2)$.

where

$$A_0^* = -\frac{1}{2}\varepsilon_0 \frac{(\varepsilon_2 - \varepsilon_1)}{\varepsilon_1 \varepsilon_2} D_0^2; \tag{C 28}$$

$$A_1^* = k\varepsilon_0 \frac{(\varepsilon_2 - \varepsilon_1)^2}{\varepsilon_1 \varepsilon_2 (\varepsilon_2 + \varepsilon_1)} \coth(kH_0) D_0^2; \tag{C 29}$$

$$A_2 = \frac{(\varepsilon_2 - \varepsilon_1)^3}{4\varepsilon_1 \varepsilon_2 (\varepsilon_2 + \varepsilon_1)^2} \left\{ -7(\varepsilon_2 + \varepsilon_1)^2 + 2(\varepsilon_2 - \varepsilon_1)^2 \right. \\ \left. \times [1 + \coth^2(kH_0) - 4 \coth(kH_0) \coth(2kH_0)] + 32\varepsilon_1 \varepsilon_2 \right\} k^2 D_0^2. \tag{C 30}$$

At the interface, the hydrostatic pressure term expresses, $p^{(2)} = -\rho_2 g y - (1/2)\varepsilon_0(1/\varepsilon_1 - 1/\varepsilon_2)D_0^2$. The equilibrium deformation is determined by the force balance, which can be written as $y_s = H_0 + B_1^* \xi e^{-jkx} + B_2^* \xi^2 e^{-2jkx}$, where

$$B_1^* = \frac{A_1^* + (\rho_2 - \rho_1)g}{\gamma k^2}; \tag{C 31}$$

$$B_2^* = \frac{A_2^*}{4\gamma k^2}. \tag{C 32}$$

For the interface in a vertical electric field, the f_y is calculated and plotted in figure 22. With the second-order term (i.e. $A_2^* \xi^2 e^{-2jkx}$) taken into account, the

electrical force does not follow the cosine function for a large deformation. Its profile is similar to the numerical results shown in figure 14. As for the equilibrium deformation, the falling part is narrow for $\varepsilon_2/\varepsilon_1 = 3$, but wide for $\varepsilon_2/\varepsilon_1 = 1 : 3$, as shown in figure 22(c,d). This is consistent with the numerical results in figure 13.

REFERENCES

- ABARZHI, S. I. 2010 Review of theoretical modelling approaches of Rayleigh–Taylor instabilities and turbulent mixing. *Phil. Trans. R. Soc. Lond. A* **368** (1916), 1809–1828.
- BARANNYK, L. L., PAPAGEORGIOU, D. T. & PETROPOULOS, P. G. 2012 Suppression of Rayleigh–Taylor instability using electric fields. *Math. Comput. Simul.* **82** (6), 1008–1016.
- BOFFETTA, G., MAZZINO, A., MUSACCHIO, S. & VOZELLA, L. 2009 Kolmogorov scaling and intermittency in Rayleigh–Taylor turbulence. *Phys. Rev. E* **79**, 065301.
- BOOMKAMP, P. A. M. & MIESEN, R. H. M. 1996 Classification of instabilities in parallel two-phase flow. *Intl J. Multiphase Flow* **22** (6), 67–88.
- CELANI, A., MAZZINO, A., MURATORE-GINANNESCHI, P. & VOZELLA, L. 2009a Phase-field model for the Rayleigh–Taylor instability of immiscible fluids. *J. Fluid Mech.* **622**, 115–134.
- CELANI, A., MAZZINO, A., MURATORE-GINANNESCHI, P. & VOZELLA, L. 2009b Rayleigh–Taylor instability in two dimensions and phase-field method. In *Advances in Turbulence XII*, pp. 169–172. Springer.
- CHANDRASEKHAR, S. 1961 *Hydrodynamic and Hydromagnetic Stability*, pp. 448–453. Clarendon.
- CHEN, S. & DOOLEN, G. D. 1998 Lattice Boltzmann method for fluid flows. *Annu. Rev. Fluid Mech.* **30** (1), 329–364.
- CHERTKOV, M. 2003 Phenomenology of Rayleigh–Taylor turbulence. *Phys. Rev. Lett.* **91** (11), 115001.
- CIMPEANU, R., PAPAGEORGIOU, D. T. & PETROPOULOS, P. G. 2014 On the control and suppression of the Rayleigh–Taylor instability using electric fields. *Phys. Fluids* **26** (2), 022105.
- CRASTER, R. V. & MATAR, O. K. 2009 Dynamics and stability of thin liquid films. *Rev. Mod. Phys.* **81** (3), 1131–1198.
- DALY, B. J. 1967 Numerical study of two fluid Rayleigh–Taylor instability. *Phys. Fluids* **10** (2), 297–307.
- DALZIEL, S. B. 1993 Rayleigh–Taylor instability: experiments with image analysis. *Dyn. Atmos. Oceans* **20** (1), 127–153.
- DIMONTE, G. 2004 Dependence of turbulent Rayleigh–Taylor instability on initial perturbations. *Phys. Rev. E* **69** (5), 056305.
- DIMONTE, G. & SCHNEIDER, M. 2000 Density ratio dependence of Rayleigh–Taylor mixing for sustained and impulsive acceleration histories. *Phys. Fluids* **12**, 304–321.
- DING, H., SPELT, P. D. & SHU, C. 2007 Diffuse interface model for incompressible two-phase flows with large density ratios. *J. Comput. Phys.* **226** (2), 2078–2095.
- GRANDISON, S., PAPAGEORGIOU, D. T. & VANDEN-BROECK, J. M. 2007 Interfacial capillary waves in the presence of electric fields. *Eur. J. Mech. (B/Fluids)* **26** (3), 404–421.
- GRANDISON, S., PAPAGEORGIOU, D. T. & VANDEN-BROECK, J. M. 2012 The influence of electric fields and surface tension on Kelvin–Helmholtz instability in two-dimensional jets. *Z. Angew. Math. Phys.* **63** (1), 125–144.
- GUERMOND, J. L. & QUARTAPELLE, L. 2000 A projection FEM for variable density incompressible flows. *J. Comput. Phys.* **165** (1), 167–188.
- HE, X., CHEN, S. & ZHANG, R. 1999 A lattice Boltzmann scheme for incompressible multiphase flow and its application in simulation of Rayleigh–Taylor instability. *J. Comput. Phys.* **152** (2), 642–663.
- HIRT, C. W. & NICHOLS, B. D. 1981 Volume of fluid (VOF) method for the dynamics of free boundaries. *J. Comput. Phys.* **39** (1), 201–225.
- HUA, J., LIM, L. K. & WANG, C.-H. 2008 Numerical simulation of deformation/motion of a drop suspended in viscous liquids under influence of steady electric fields. *Phys. Fluids* **20** (11), 113302.

- JACKSON, J. D. 1999 *Classical Electrodynamics*. Wiley.
- JACQMIN, D. 1999 Calculation of two-phase Navier–Stokes flows using phase-field modeling. *J. Comput. Phys.* **155** (1), 96–127.
- JOSHI, A., RADHAKRISHNA, M. C. & RUDRAIAH, N. 2010 Rayleigh–Taylor instability in dielectric fluids. *Phys. Fluids* **22** (6), 064102.
- KILKENNY, J. D., GLENDINNING, S. G., HAAN, S. W., HAMMEL, B. A., LINDL, J. D., MUNRO, D., REMINGTON, B. A., WEBER, S. V., KNAUER, J. P. & VERDON, C. P. 1994 A review of the ablative stabilization of the Rayleigh–Taylor instability in regimes relevant to inertial confinement fusion. *Phys. Plasmas* **1** (5), 1379–1389.
- KOROVIN, V. M. 2011 Effect of tangential electric field on the evolution of the Rayleigh–Taylor instability of a dielectric liquid film. *Tech. Phys.* **56** (10), 1390–1397.
- KULL, H. J. 1991 Theory of the Rayleigh–Taylor instability. *Phys. Rep.* **206** (5), 197–325.
- LAYZER, D. 1955 On the instability of superposed fluids in a gravitational field. *Astrophys. J.* **122**, 1.
- LEE, H. G., KIM, K. & KIM, J. 2011 On the long time simulation of the Rayleigh–Taylor instability. *Intl J. Numer. Meth. Engng* **85** (13), 1633–1647.
- LIN, Y., SKJETNE, P. & CARLSON, A. 2012 A phase field model for multiphase electro-hydrodynamic flow. *Intl J. Multiphase Flow* **45**, 1–11.
- MELCHER, J. R. & SCHWARZ, W. J. JR 1968 Interfacial relaxation overstability in a tangential electric field. *Phys. Fluids* **11** (12), 2604–2616.
- MICHIOKA, H. & SUMITA, I. 2005 Rayleigh–Taylor instability of a particle packed viscous fluid: implications for a solidifying magma. *Geophys. Res. Lett.* **32** (3), L03309.
- MOHAMED, A. & EL SHEHAWAY, E. S. F. 1983a Nonlinear electrohydrodynamic Rayleigh–Taylor instability. II: a perpendicular field producing surface charge. *Phys. Fluids* **26** (7), 1724–1730.
- MOHAMED, A. E. M. A. & SHEHAWAY, E. S. F. 1983b Nonlinear electrohydrodynamic Rayleigh–Taylor instability. Part I. A perpendicular field in the absence of surface charges. *J. Fluid Mech.* **129**, 473–494.
- OLSON, D. H. & JACOBS, J. W. 2009 Experimental study of Rayleigh–Taylor instability with a complex initial perturbation. *Phys. Fluids* **21** (3), 034103.
- RAHMAT, A., TOFIGHI, N., SHADLOO, M. S. & YILDIZ, M. 2014 Numerical simulation of wall bounded and electrically excited Rayleigh–Taylor instability using incompressible smoothed particle hydrodynamics. *Colloid Surf. A* **460**, 60–70.
- RAMAPRABHU, P., DIMONTE, G., WOODWARD, P., FRYER, C., ROCKEFELLER, G., MUTHURAMAN, K., LIN, P.-H. & JAYARAJ, J. 2012 The late-time dynamics of the single-mode Rayleigh–Taylor instability. *Phys. Fluids* **24** (7), 074107.
- RAYLEIGH, LORD 1883 Investigation of the character of the equilibrium of an incompressible heavy fluid of variable density. *Proc. Lond. Math. Soc.* **14**, 170–177.
- RAYLEIGH, LORD 1900 *Scientific Papers*. vol. II. Cambridge University Press.
- RENOULT, M. C., PETSCHKE, R. G., ROSENBLATT, C. & CARLÈS, P. 2011 Deforming static fluid interfaces with magnetic fields: application to the Rayleigh–Taylor instability. *Exp. Fluids* **51** (4), 1073–1083.
- RIBEYRE, X., TIKHONCHUK, V. T. & BOUQUET, S. 2004 Compressible Rayleigh–Taylor instabilities in supernova remnants. *Phys. Fluids* **16** (12), 4661–4670.
- SAVILLE, D. A. 1997 Electrohydrodynamics: the Taylor–Melcher leaky dielectric model. *Annu. Rev. Fluid Mech.* **29**, 27–64.
- SCHNEIDER, M. B., DIMONTE, G. & REMINGTON, B. 1998 Large and small scale structure in Rayleigh–Taylor mixing. *Phys. Rev. Lett.* **80** (16), 3507.
- SHARP, D. H. 1984 An overview of Rayleigh–Taylor instability. *Physica D* **12** (1), 3–18.
- SOHN, S. I. 2009 Effects of surface tension and viscosity on the growth rates of Rayleigh–Taylor and Richtmyer–Meshkov instabilities. *Phys. Rev. E* **80** (5), 055302.
- TAYLOR, G. 1950 The instability of liquid surfaces when accelerated in a direction perpendicular to their planes. I. *Proc. R. Soc. Lond. A* **201** (1065), 192–196.

- TAYLOR, G. I. & MCEWAN, A. D. 1965 The stability of a horizontal fluid interface in a vertical electric field. *J. Fluid Mech.* **22** (01), 1–15.
- THORPE, A. J., VOLKERT, H. & ZIEMIANSKI, M. J. 2003 The Bjerknes' circulation theorem: a historical perspective. *Bull. Am. Meteorol. Soc.* **4**, 471–480.
- TOMAR, G., GERLACH, D., BISWAS, G., ALLEBORN, N., SHARMA, A., DURST, F., WELCH, S. W. J. & DELGADO, A. 2007 Two-phase electrohydrodynamic simulations using a volume-of-fluid approach. *J. Comput. Phys.* **227** (2), 1267–1285.
- TRYGGVASON, G. 1988 Numerical simulations of the Rayleigh–Taylor instability. *J. Comput. Phys.* **75** (2), 253–282.
- WHITE, J., OAKLEY, J., ANDERSON, M. & BONAZZA, R. 2010 Experimental measurements of the nonlinear Rayleigh–Taylor instability using a magnetorheological fluid. *Phys. Rev. E* **81** (2), 026303.
- WU, N. & RUSSEL, W. B. 2009 Micro- and nano-patterns created via electrohydrodynamic instabilities. *Nano Today* **4** (2), 180–192.
- YANG, Q., LI, B. Q. & DING, Y. 2013 3D phase field modeling of electrohydrodynamic multiphase flows. *Intl J. Multiphase Flow* **57**, 1–9.
- YANG, Q., LI, B. Q., SHAO, J. & DING, Y. 2014 A phase field numerical study of 3D bubble rising in viscous fluids under an electric field. *Intl J. Heat Mass Transfer* **78**, 820–829.
- YIH, C. S. 1967 Instability due to viscosity stratification. *J. Fluid Mech.* **27** (02), 337–352.
- YOUNGS, D. L. 1984 Numerical simulation of turbulent mixing by Rayleigh–Taylor instability. *Physica D* **12** (1), 32–44.